PHYSICAL REVIEW D **94,** 034007 (2016)

Aspects of perturbative QCD at a 100 TeV future hadron collider

Enrico Bothmann,[1] Piero Ferrarese,[1] Frank Krauss,[2] Silvan Kuttimalai,[2] Steffen Schumann,[1] and Jennifer Thompson[1]

[1]*II. Physikalisches Institut Universität Göttingen, Friedrich-Hund-Platz 1, 37077 Göttingen, Germany*

[2]*Institute for Particle Physics Phenomenology, Durham University, Durham DH1 3LE, UK*

(Received 6 May 2016; published 4 August 2016)

In this paper we consider particle production at a future circular hadron collider with 100 TeV center-of-mass energy within the Standard Model, and in particular their QCD aspects. Accurate predictions for these processes pose severe theoretical challenges related to large hierarchies of scales and possible large multiplicities of final-state particles. We investigate scaling patterns in multijet-production rates allowing to extrapolate predictions to very high final-state multiplicities. Furthermore, we consider large-area QCD jets and study the expectation for the mean number of subjets to be reconstructed from their constituents and confront these with analytical resummed predictions and with the expectation for boosted hadronic decays of top quarks and W bosons. We also discuss the validity of Higgs effective field theory in making predictions for Higgs-boson production in association with jets. Finally, we consider the case of new physics searches at such a 100 TeV hadron-collider machine and discuss the expectations for corresponding Standard-Model background processes.

DOI: 10.1103/PhysRevD.94.034007

I. INTRODUCTION

The first run at the Large Hadron Collider (LHC-Run I) was a great success. This is best exemplified with the discovery of the Higgs boson by the ATLAS and CMS collaborations [1,2]. As a concrete manifestation of the Brout-Englert-Higgs (BEH) mechanism of electroweak symmetry breaking, this boson is responsible for the generation of elementary masses [3–6]. Its discovery ultimately completed the triumph of the gauge principle as the paradigm underlying our highly detailed understanding of all fundamental interactions at the particle level apart from gravitation. It is obvious that after this discovery further runs at the LHC will concentrate on further studies of this newly found particle. The determination of its quantum numbers and couplings to other particles in the Standard Model (SM) through an analysis of various combinations of production and decay channels will definitely shed additional light on its true nature. In particular, a careful analysis of the pattern of its couplings to other particles will clarify if it is indeed the Higgs boson in the minimal realization of the Standard Model or if it opens the opportunity to study new phenomena beyond it. Examples for such new phenomena include the following:

(i) Possible new dynamics, in particular involving the electroweak sector of the Standard Model and the symmetry breaking through the Higgs potential.

An integral part of the BEH mechanism is the quartic Higgs potential. This potential most unambiguously manifests itself in the self-interactions of the Higgs boson. Higgs pair production will allow some initial, rough tests of this potential at forthcoming runs of the LHC, and it will start constraining potential new operator structures of higher dimension stemming from extended sectors at larger scales. At higher energies, this program can be further extended through more precise tests of the pair production or through triple Higgs production processes, which may be susceptible to further, additional operators. In a similar way, multiple gauge boson production, especially at high energies, offers ample opportunities to study and constrain higher-dimensional operators—a program which, of course, has been pursued for decades now.

(ii) Unitarity of the Standard Model at the highest energies.

Interactions between the Higgs, the gauge and the fermion sector exhibit subtle relations in order to guarantee the unitarity of cross sections. At increasingly higher energies these relations can be subjected to increasingly stringent tests, in particular in those processes where various final states emerge in the fusion of electroweak gauge bosons.

(iii) The persistent hierarchy problem and its consequences.

Especially after the discovery of the Higgs boson with its relatively close resemblance to its realization in the SM, it is staggering how large quantum corrections to its mass, which are directly sensitive to the ratio of the scale related to a more complete model of nature and the actual electroweak symmetry breaking scale, can be absorbed in such a stable way. Many mechanisms have been suggested to cover the apparent void between these scales and to stabilize the effective theory that the SM is, with supersymmetry being the most prominent. Up to now, no realization of such models for new physics has been discovered, and with only few exceptions

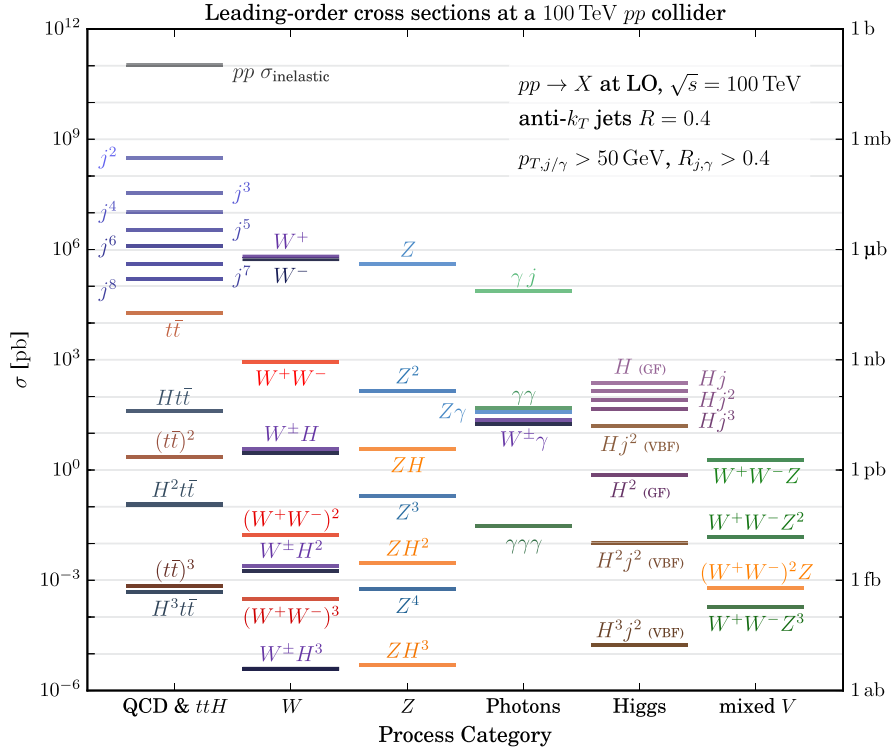

FIG. 1. A compilation of LO inclusive production cross sections at the 100 TeV future pp collider. The Higgs cross sections labelled with "GF" refer to Higgs production via gluon fusion, whereas "VBF" stands for vector-boson fusion production. For gluon fusion Higgs production the top mass effects have been included; see Sec. IV.

any hints indicating a discovery have not stood the test of time and have disappeared.

Questions like the ones outlined above can be studied by pushing the energy frontier of hadron colliders. It is thus not surprising that discussions already have started concerning such a machine [7]. As a typical setup, hadronic center-of-mass energies of 100 TeV in pp collisions are assumed with an anticipated luminosity of 1–10 ab^{-1} [7–9].

In order to gain some intuition about the kind of *known* physics that will be encountered at such a machine, representative cross sections for the production of relevant high-multiplicity final states are compiled in Fig. 1. The first thing to notice is the inelastic cross section at the future circular hadron collider (FCC), being around 105 mb [10], which constitutes a 45% increase compared to the LHC (~72 mb). To contrast that, we calculated leading-order (LO) cross sections for a multitude of processes, with cross sections ranging from a few attobarn up to hundreds of microbarn, across 15 orders of magnitude. QCD-only processes come with the largest cross sections when a jet cut of $p_{T,\mathrm{min}} = 50$ GeV is used, with dijet production at 315 μb. Also higher jet multiplicities have very high cross sections, and only inclusive seven-jet production is less probable than any other hard process: the inclusive single vector-boson production cross sections come with 350–600 nb and are thus slightly enhanced compared to seven-jet production. The least probable cross sections included in Fig. 1 are those of triple Higgs production in association with a vector boson or from vector-boson fusion (VBF) with at least two jets. These cross sections are between 3 and 20 ab. Thus at least the $H^3 j^2$ cross section would still correspond to several events at a luminosity of 1–10 ab^{-1}.

In this paper we want to address some of the challenges of QCD production processes at a 100 TeV hadron collider. We first discuss, in Sec. II, in some detail the scaling behavior in the production of final states involving many jets, using pure QCD multijet production and vector-boson production associated with jets as typical benchmarks for this part of SM dynamics. We discuss the scaling in jet multiplicities between 14 and 100 TeV, and the scaling behavior in ratios of multijet cross sections, which differ by one in the jet multiplicity. The latter is particularly interesting, since increasing collider energies allow increasingly more hierarchical kinematical situations, which in turn trigger the transition of the well-known staircase scaling—also known as Berends scaling—to a Poissonian scaling. The latter is usually associated with the onset of practically unconstrained, independent emission patterns. We continue our investigations in Sec. III with a related topic, namely the jetty substructure emerging in the production and decay of heavily boosted unstable particles, such as top quarks or gauge bosons. Here, we use

analytic results and contrast them with the results in our simulation. We change gears in Sec. IV, and quantify finite mass effects in loop-initiated processes. Due to the large gluon parton distribution function (PDF), such processes become increasingly important at higher energies, and the large energies also allow for scales well above the top-mass threshold to be tested, which in turn leads to jet transverse momentum distributions which are notably different from expectations driven by effective theories. Finally, in Sec. V we discuss the SM backgrounds for typical signatures used in searches for new physics.

A. Calculational baseline

In our studies we use different parts of event simulation tools, which are available in practically all modern Monte Carlo event generators [11]. Their accuracy reflects our detailed understanding of the dynamics of the Standard Model, and in particular, of QCD. Their predictions have been confronted with LHC data in many studies; for a recent review see Ref. [12]. In particular, methods developed to automate the evaluation of QCD one-loop corrections [13–18], and the techniques used to interface such exact, fixed-order matrix elements with parton showers [19–24], buttress the unprecedented level of accuracy in our simulations. But of course, an extrapolation by about an order of magnitude in the center-of-mass energy from LHC energies to the 100 TeV scale is plagued with uncertainties and potential shortcomings:

(i) First of all, it is not entirely unlikely that the current PDFs, including the gluon, the photon and all quarks up to the bottom quark, must be extended to include also W and Z bosons or even the top quark. While this sounds a bit strange at first, it is worth pointing out that the question of whether such objects must be included is synonymous with whether partonic scales $\hat{E}$ are probed that yield large logarithms of the type $\log(\hat{E}/M)$, where M is the mass of the heavy object. And, similar to the LHC probing the TeV scale and thereby rendering $\log(1\ \mathrm{TeV}/m_b)$ a possibly large logarithm, a 100 TeV machine will probe scales up to around 20 TeV and thereby $\log(20\ \mathrm{TeV}/M)$ with $M = m_W,\ m_Z,\ m_t$ will be as large.

(ii) Vaguely related to this issue is the question concerning the correct factorization scheme, in particular for processes like jet production with jet transverse momenta of 100 GeV or below. A simple calculation shows that with such processes the PDFs are probed at x ranges of $x \approx 10^{-5}$ or below, which is typically identified as a kinematical regime where the conventional collinear factorization and its DGLAP scaling might not yield correct results, and one would have to resort to the BFKL picture or something similar. This then would also mean that different factorization schemes, such as $k_\perp$ factorization, would have to be invoked. In this paper, however, only conventional collinear factorization will be used.

(iii) In a similar way, one could argue that our knowledge of multiple parton interactions is fairly limited. The conventional picture of such multiple scatterings is based on a simple factorization, which appears to hold true at the LHC. A similar picture of typically more or less uncorrelated parton-parton scattering processes is also successfully employed in Monte Carlo simulations programs like PYTHIA [25], HERWIG [26], or SHERPA [27,28] to drive what is known as the underlying event. On the other hand, this relatively simple picture cannot be entirely true, and at high energies correlation effects, parton rescattering, the interplay between different scatters etc. will become important.

These issues render the naive extrapolation of current models a probably too optimistic procedure, and therefore, in this paper, we concentrate on observables expected to be largely insensitive to multiple parton scattering.

For the following studies, the SHERPA event generation framework has been used. Proton-proton collisions at center-of-mass energies of 100 TeV are considered and, in relevant cases, compared to collisions at LHC Run II energies of 14 TeV, to highlight interesting features of energy scaling and similar features. If not stated otherwise, jets are reconstructed with the anti-k_T algorithm with a radius parameter of $R = 0.4$, using the FASTJET package [29,30]. For matrix element generation and cross-section calculations at leading order COMIX [31] is employed. The NNPDF3.0 next-to-leading-order (NLO) PDF set [32] is used, which also provides the strong coupling α_s. Renormalization and factorization scales are defined in a process-specific way, they are listed separately in the respective subsections. For most distributions, the multijet-merging technology developed in Refs. [19,33,34][1] is employed. We use the parton shower built on Catani-Seymour subtraction kernels as proposed in Ref. [42] and implemented in Ref. [43]. The inclusion of higher-order accuracy in the parton shower simulations is facilitated by either the MC@NLO method [20] in the SHERPA version [23,44,45] or by the multijet merging at NLO [46,47].[2] For the modelling of nonperturbative effects, SHERPA's in-built hadronization [50], underlying event model [51], hadron decays and QED final-state radiation [52] modules have

[1] It is worth noting that other merging techniques exist, like for instance those described in Refs. [35–40], which however by and large have been shown to yield comparable results at lower energies; see for example Ref. [41].

[2] For the matching of NLO matrix elements with parton showers and the merging with matrix elements for higher jet multiplicities, other methods have been described in Refs. [21,24,48,49].

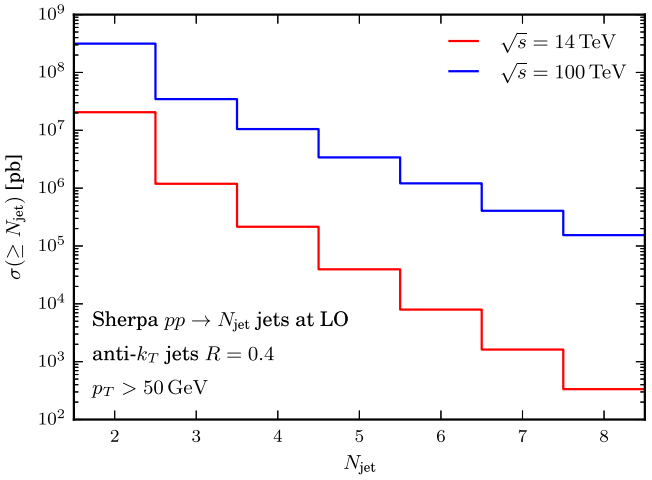

FIG. 2. A comparison of LO QCD production rates of at least N_{jet} anti-k_T jets with $p_T > 50$ GeV and $R = 0.4$ in proton-proton collisions at $\sqrt{s} = 14$ TeV and $\sqrt{s} = 100$ TeV.

been used. The Standard Model input parameters are defined through the G_μ scheme with

$$m_Z = 91.188\ \text{GeV}, \qquad \Gamma_Z = 2.49\ \text{GeV}, \tag{1.1}$$

$$m_W = 80.419\ \text{GeV}, \qquad \Gamma_W = 2.06\ \text{GeV}, \tag{1.2}$$

$$m_H = 125\ \text{GeV}, \qquad \Gamma_H = 0.00407\ \text{GeV}, \tag{1.3}$$

$$m_t = 175\ \text{GeV}, \qquad \Gamma_t = 1.5\ \text{GeV}, \tag{1.4}$$

$$G_\mu = 1.16639 \times 10^{-5}\ \text{GeV}^{-2}, \qquad \sin^2\theta_W = 1 - M_W^2/\tilde{M}_Z^2 \tag{1.5}$$

and the complex-mass scheme [53] is used. Apart from the top quark, all other quarks are assumed massless, and top-quark mass effects are included in the running of α_s.

II. SCALING PATTERNS IN JETS AND V + JETS PRODUCTION

When considering hadron collisions at very high energies, QCD jet production processes are omnipresent. Even processes with very large multiplicity of (associated) jets exhibit sizable rates. Accurate predictions for such final states pose a severe challenge for Monte Carlo event generators and one might have to resort to approximate methods. This section focuses on one such approach, which is based on the scaling behavior of QCD jet rates with respect to jet multiplicity.

To give an impression of jet-production rates at the FCC, Fig. 2 compares the leading-order multijet cross sections at hadronic collision energies of $\sqrt{s} = 14$ TeV (LHC) and $\sqrt{s} = 100$ TeV (FCC). For these estimates, anti-k_T jets with $R = 0.4$ and a minimal jet transverse momentum of $p_{T,\text{min}} = 50$ GeV are considered. While the two-jet cross section increases by 1 order of magnitude, an increase of more than 2 orders of magnitude for the production of at least eight jets is to be expected. In absolute numbers, the total LO dijet rate at the FCC is of order 300 μb while the LO eight-jet cross section for jets with transverse momentum above 50 GeV amounts to 150 nb.

In Fig. 3, anti-k_T jet rates at NLO QCD differential in jet transverse momentum and additionally binned in jet rapidity y are presented. Results have been obtained with BLACKHAT+SHERPA [54]; both the renormalization and factorization scale have been set to $\mu_R = \mu_F = \frac{1}{2}H_T$. Comparing rates for 14 and 100 TeV center-of-mass energy, an increase of about 1 order of magnitude for central jets with low and moderate p_T is observed. This effect becomes more extreme at larger p_T values; for example at $p_T = 3.5$ TeV the FCC rates are more than 3 orders of magnitude larger than at the LHC. In fact, the FCC provides substantial jet rates even for very large rapidities: 200 GeV jets with $5 < |y| < 6$ come with rates about 2 orders of magnitude larger than those for 200 GeV jets in the more central $4 < |y| < 5$ bin at the LHC. From

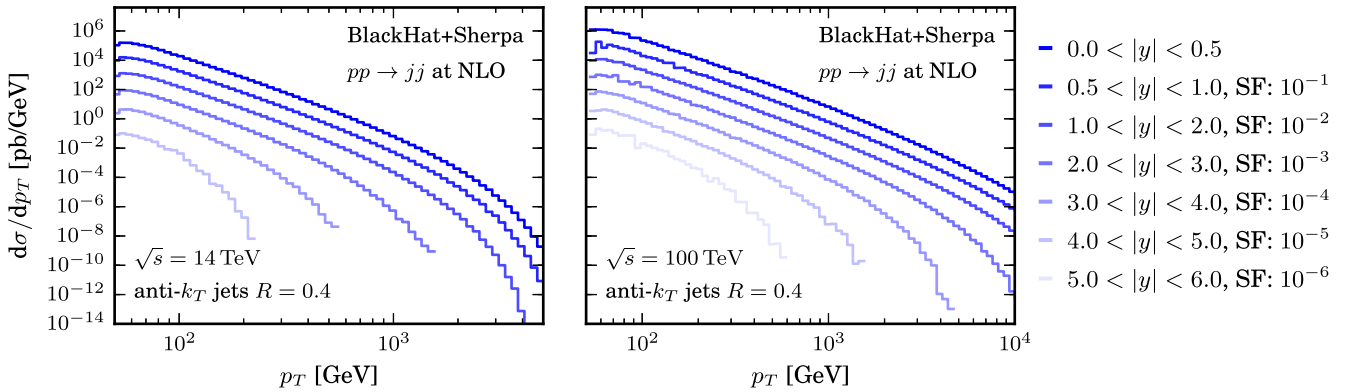

FIG. 3. NLO QCD inclusive jet cross sections for LHC (left) and FCC (right) collision energies, differential in p_T for different bins in jet rapidity y. Note that for illustrative purposes results have been multiplied by variable scaling factors (SF), as indicated in the legend.

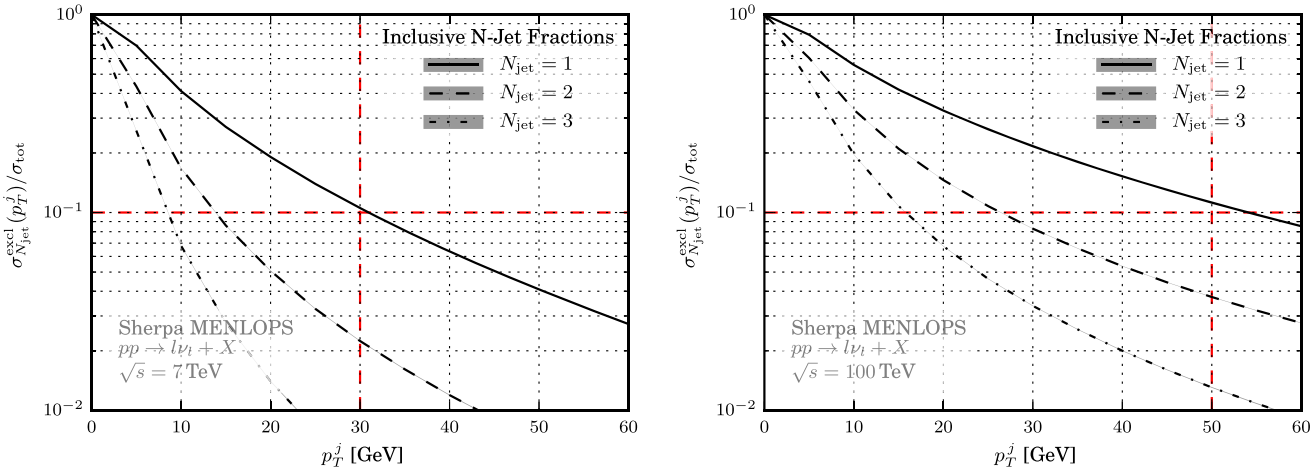

FIG. 4. Normalized jet rates for different inclusive jet multiplicities differential in jet p_T for $W+$ jets production at the LHC and the FCC. The dashed red lines indicate the effect of cutting at $p_{T,\text{min}}^{\text{jet}} = 30$ GeV, i.e. 50 GeV.

these rate estimates, it can be concluded that one can expect at least 10 times more jets at the FCC than at the LHC. This massive enhancement will become even larger in high-p_T and/or high-$|y|$ regions or when demanding large jet multiplicities. Accordingly, the rapidity coverage of general-purpose detectors at the FCC should increase with respect to ATLAS or CMS.

So far, identical jet-selection criteria, and in particular p_T thresholds, have been considered, both for the LHC and the FCC machine. However, moving to a 100 TeV collider will certainly entail adjustments in the jet-cut choices. At LHC in analyses looking for new physics, typical jet $p_{T,\text{min}}$ cuts often are around 25–30 GeV. To gain some insight into which range of $p_{T,\text{min}}$ cuts would lead to a similar relative suppression of low-p_T jets at the FCC as using 25–30 GeV produces at the LHC, one could use a standard candle such as $W+$ jets production. In Fig. 4, inclusive jet fractions in $W+n$-jet production, differential in $p_{T,\text{min}}$, are presented for the 7 TeV LHC and the 100 TeV FCC setup. A jet transverse momentum cut of $p_{T,\text{min}} = 50$ GeV at the FCC leads to a one-jet inclusive fraction of order 10%, similar to the effect of a $p_{T,\text{min}} = 30$ GeV cut at the 7 TeV LHC. Accordingly, in what follows a p_T threshold of 50 GeV will be considered unless explicitly stated otherwise.

The QCD jet production rates to be anticipated at the FCC demand suitable theoretical methods even for very large jet multiplicities. While fixed-order predictions for given jet processes are suitable to describe the corresponding jet-multiplicity bin, matrix-element parton-shower merging techniques provide inclusive predictions, differential in the jet multiplicity, with high jet multiplicities beyond the reach of fixed-order technology being modeled through the parton shower. Alternatively, there has recently been progress in making (semi)analytical predictions for jet rates at hadron colliders that account for small jet radii and high jet counts [55–57]. With the advent of such methods, the morphology of the entire jet-multiplicity distribution can be studied. Guided by phenomenological evidence, and supported by both fixed-order calculations and parton-shower simulations, certain jet-multiplicity scaling patterns can be identified [58] that find their analogue in the analytical jet-rate predictions [55,56]. As already visible in Fig. 2, jet rates differential in the number of jets exhibit a high degree of regularity. To study this feature one considers the ratio $R_{(n+1)/n}$ of the exclusive $n+1$ over the n-jet cross section, i.e.

$$R_{(n+1)/n} \equiv \frac{\sigma_{n+1}^{\text{excl}}}{\sigma_n^{\text{excl}}}. \tag{2.1}$$

The approximately equal step size (on a logarithmic scale) between subsequent exclusive jet rates observed in Fig. 2 translates into a flat plateau for $R_{(n+1)/n}$, i.e. $R_{(n+1)/n} \sim$ constant. This implies a simple exponential form of the jet-rate distribution, also known as the staircase pattern. A second possibility for the jet-rate distributions is the Poissonian pattern. Jet cross sections following a simple Poisson statistics result in $R_{(n+1)/n} \sim \bar{n}/(n+1)$, with the average number of jets given by $\bar{n}$.

Both these patterns have been observed in LHC data [59–62] and in Monte Carlo studies [63–65]. They can be understood as the limiting cases for the jet-emission probability: for $\alpha_s/\pi \log^2 Q/Q_0 \ll 1$ a staircase-like pattern is induced while for $\alpha_s/\pi \log^2 Q/Q_0 \gg 1$ a Poisson-scaling pattern is found [55,58,66]. Here Q denotes the hard process scale and Q_0 is of the order of the jet-resolution scale, i.e. $Q_0 \sim p_{T,\text{min}}$. The derivation is based on the language of generating functionals for the jet rates. The two distinct regimes correspond to additional parton emissions being distributed either equally among all other partons or

stemming predominantly from a single hard parton line. The latter follows a simple Sudakov decay-like model which results in a Poisson distribution, as it is the case for photon emissions from a hard electron line [67]. The case of democratic emissions (mainly gluons from gluons), on the other hand, is exclusive to field theories with a non-Abelian group structure as in QCD.

In realistic measurements, jet patterns will be overlaid and cut off by other effects, such as phase-space constraints. When the available energy for further jet emission is depleted or jets already radiated cover a good fraction of the available solid angle [66], then higher multiplicities will quickly tend to zero. On the other hand, the first few emissions carry away sizable parts of the total energy available, such that the increase in the partonic momentum fractions at which any participating PDFs are evaluated is comparably large. This leads to a somewhat steeper decrease of jet rates for the first few emissions and is known as the PDF suppression effect [58]. Furthermore, the described regimes represent limiting cases and one can expect a transition from the Poisson scaling to the staircase scaling when the jet evolution begins to wash out any initial large scale hierarchy [55]. When ultimately the energy of the partons in the jet evolution becomes of order Q_0, one expects such patterns to break down giving way to a faster reduction of higher multiplicities.

In view of the enormous phase space available for producing additional jets at the FCC collider, studies of the jet multiplicity distribution based on scaling patterns will provide a sensitive handle to estimate and probe the tails of the distribution, where otherwise one has to largely rely on parton-shower simulations alone. Based on these predictions, background subtractions for new physics signatures resulting from decays of new heavy colored particles yielding a distinct imprint on the multiplicity distribution might become feasible [63,68].

To study how well simple jet scaling patterns describe the jet-multiplicity distributions at FCC energies, fits of $R_{(n+1)/n}$ in Monte Carlo predictions are considered. For that purpose, Monte Carlo samples for pure jet production and vector-boson production are explored, triggering scaling patterns using either democratic or hierarchical, i.e. staggered, jet cuts. Here *democratic* reflects the fact that all jet $p_{T,\mathrm{min}}$ are of the same order, i.e. uniform, whereas *hierarchical* refers to the scenario where the cut on the leading jet, $p_{T,\mathrm{min}}^{\mathrm{leading}}$, is significantly increased.

The cut scenarios considered for pure jet production are listed in Table I. In all cases the $2 \to 2$ core process has been considered at MCNLO@NLO accuracy; furthermore LO matrix elements for final-state multiplicities up to six partons are included, all consistently merged with the parton shower. In Fig. 5 the resulting $R_{(n+1)/n}$ distributions are presented for the four considered selections. Note, the index n counts the number of jets radiated off the hard two-to-two core, i.e. $n = 1$ corresponds to the production of three final-state jets.

As discussed in Ref. [64], jets assigned to the core process behave differently from jets emitted thereof, which is why they have to be dismissed from pattern fits through the data. Furthermore, PDF effects leave a nonuniversal imprint on the first few bins. Therefore, for the staircase-like patterns found for the democratic cut scenarios, cf. the two upper panels of Fig. 5, the fits are based on the values from $R_{4/3}$ through $R_{6/5}$. For the hierarchical cut scenarios, PDF suppression effects are less prominent, due to hard cuts on the leading jet that induces a much higher scale Q for the core process. Accordingly, the fits for the Poisson-like patterns, cf. the two lower panels in Fig. 5, are based on $R_{2/1}$ up to $R_{6/5}$. To quantify the quality of the fits, terms linear in n for the staircase pattern and a constant term for the Poisson pattern have been added to the ideal scaling hypotheses. The resulting fit functions for the two scenarios read

$$f_{\mathrm{Staircase}}(n) = c + mn, \tag{2.2}$$

$$f_{\mathrm{Poisson}}(n) = \frac{\bar{n}}{n+1} + c. \tag{2.3}$$

All resulting fit parameters are listed in Table I. For all cut scenarios the fit function and its extrapolation to higher jet bins describe the simulated data very well. For the two democratic scenarios, the constant c decreases from 0.35 to 0.29 when we increase the jet cuts, reflecting the fact that the *cost* for adding an additional jet gets higher.

Poissonian emission patterns are obtained when hierarchical cuts are applied. Although the constant offset, c, increases from 0.16 to 0.25 when enlarging the gap

TABLE I. The jet-cut scenarios considered for pure jet production at FCC energies. Furthermore, the fit hypothesis used, cf. Eqs. (2.2) and (2.3), and the corresponding parameters are listed.

label	$p_{T,\mathrm{min}}^{\mathrm{leading}}$ [GeV]	$p_{T,\mathrm{min}}$ [GeV]	fit function	fit region	fit parameters
S1 (democratic)	100	50	$f_{\mathrm{Staircase}}$	$3 \le n \le 5$	$c = 0.342$, $m = 0.006$
S2 (democratic)	200	100	$f_{\mathrm{Staircase}}$	$3 \le n \le 5$	$c = 0.274$, $m = 0.003$
P1 (hierarchical)	500	50	f_{Poisson}	$1 \le n \le 5$	$\bar{n} = 2.21$, $c = 0.16$
P2 (hierarchical)	2000	50	f_{Poisson}	$1 \le n \le 5$	$\bar{n} = 2.64$, $c = 0.25$

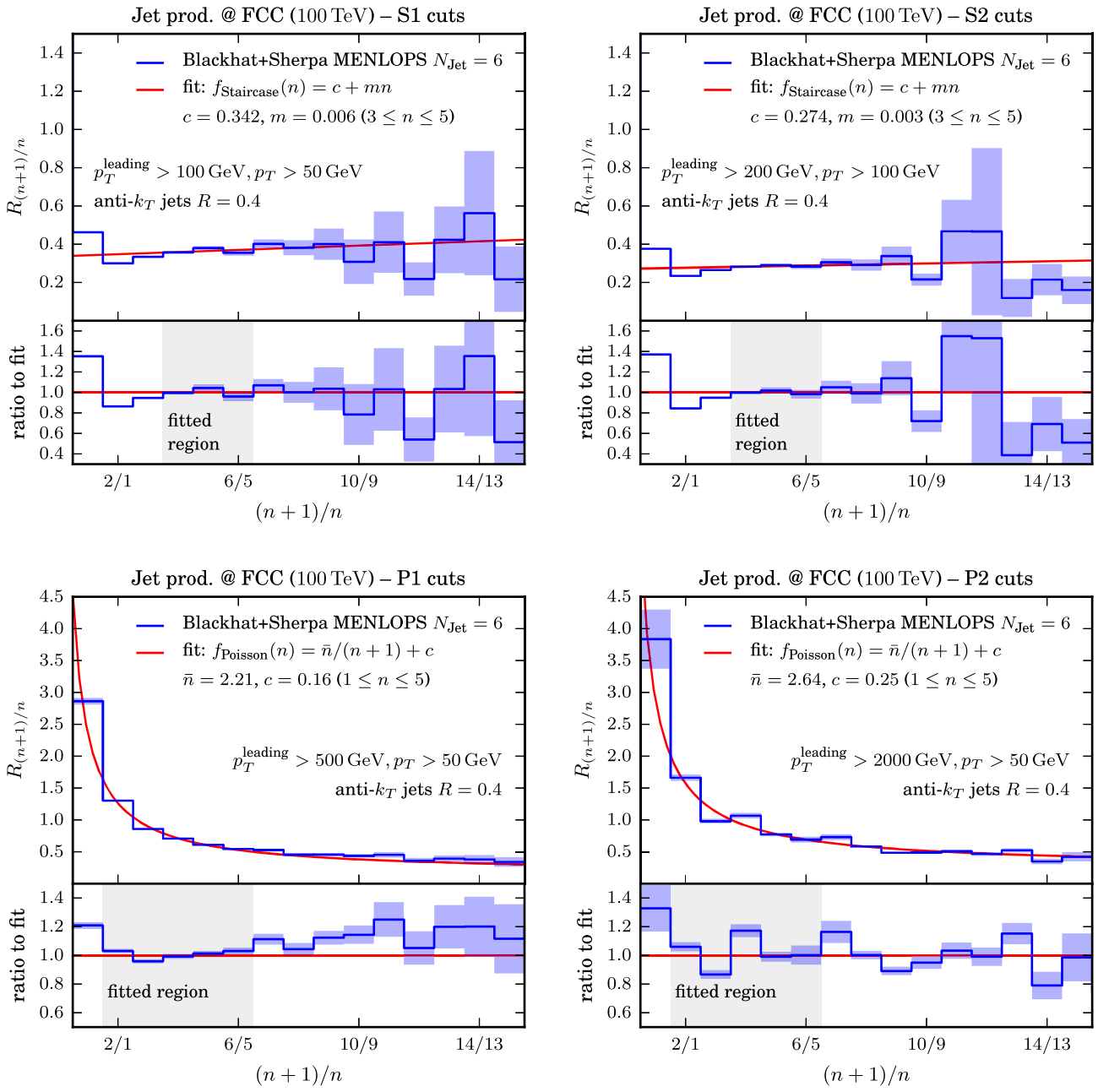

FIG. 5. The exclusive jet multiplicity ratio $R_{(n+1)/n}$ in pure jet production at the FCC. Results are presented for the four cut scenarios described in Table I with fits for the staircase and Poisson patterns, cf. Eqs. (2.2) and (2.3).

between the leading jet cut and the overall jet cut $p_{T,\text{min}}$, one can see by eye that the fit quality is better for the larger cut gap, i.e. 2000 GeV vs 50 GeV. For the smaller cut gap, i.e. 500 GeV vs 50 GeV, the fit increasingly underestimates $R_{(n+1)/n}$ for growing n, which might indicate a faster transition to a more staircase-like behavior. As expected, the average jet multiplicity $\bar{n}$ found from the fit increases with a larger leading jet cut (from 2.2 to 2.6). In particular the S2 and P2 cut scenarios are very well modeled by the simple scaling-pattern hypotheses and allow for reliable extrapolations where explicit calculations-based and fixed-order or even parton-shower simulations become computationally unfeasible.

As explained above, jet-multiplicity scaling patterns are a generic feature of associated jet-production processes. To illustrate this, vector-boson production, and in particular W-boson production, in association with jets will be considered in the following. Once again, samples based on an MCNLO@NLO simulation of $pp \to W$ merged with additional LO matrix elements for up to five jets dressed with parton showers have been produced. In Fig. 6, the predictions for exclusive jet rates imposing a jet cut of

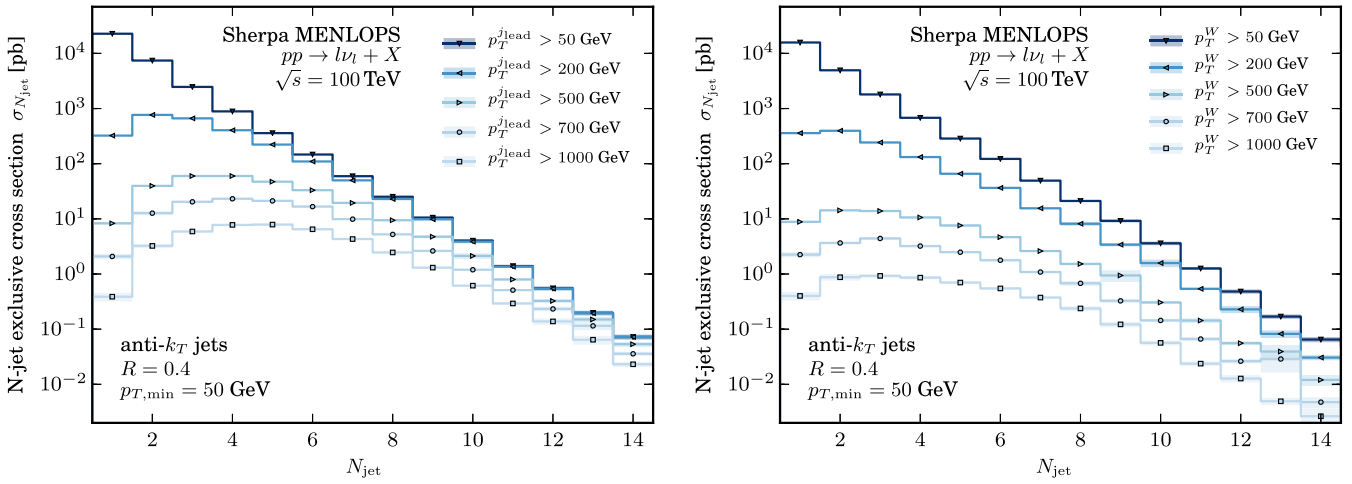

FIG. 6. Exclusive jet rates for W-boson production in association with n jets for different cuts on the leading jet (left panel) and the W-boson (right panel) transverse momentum, respectively. For all (subsequent) jets the universal cut of $p_T > 50$ GeV is applied.

$p_{T,\text{min}} = 50$ GeV and variable cuts on the leading jet (left panel) or on the W-boson (right panel) transverse momentum are presented. The two cut schemes induce very similar shapes of the multiplicity distributions but the overall rates are significantly smaller when demanding the W boson to have large transverse momentum. In fact, a sizable part of the $W +$ jets cross section originates from hard jets accompanied by a vector boson with comparatively low transverse momentum [69].

For comparison, Fig. 7 shows the same event selections but for a pure MC@NLO simulation of the inclusive vector-boson production process, i.e. without any additional tree-level matrix elements taken into account. Noticeably, with the lack of higher-multiplicity matrix elements the rate estimates for the high-multiplicity bins are orders of magnitude smaller than in the merged run. From similar comparisons at LHC energies, it is apparent that the predictions based on higher-multiplicity matrix elements are more reliable and describe data much better; see for instance Refs. [60–62,70].

In Figs. 8 and 9, the exclusive jet multiplicity ratios $R_{(n+1)/n}$ for the multijet-merged sample described above are plotted alongside fits following the functional forms given in Eqs. (2.2) and (2.3). In this context, the jet multiplicity, n, counts the number of jets in addition to the core process $pp \to l\nu_l + j$, i.e. W production in association with at least one jet. In Fig. 8 results for the democratic selection scenario, i.e. a universal jet cut of $p_{T,\text{min}} = 50$ GeV, requiring $p_{T,W} > 100$ GeV, are presented. A fit of the staircase hypothesis in the range $1 \leq n \leq 5$ results in an almost vanishing parameter m. This presents an ideal staircase scaling, with a constant ratio of $c = 0.4$. The extrapolation of this scaling function to higher values of n is in very good agreement with the Monte Carlo simulation results. In Fig. 9, the corresponding results for hierarchical selection criteria are presented. Two cut

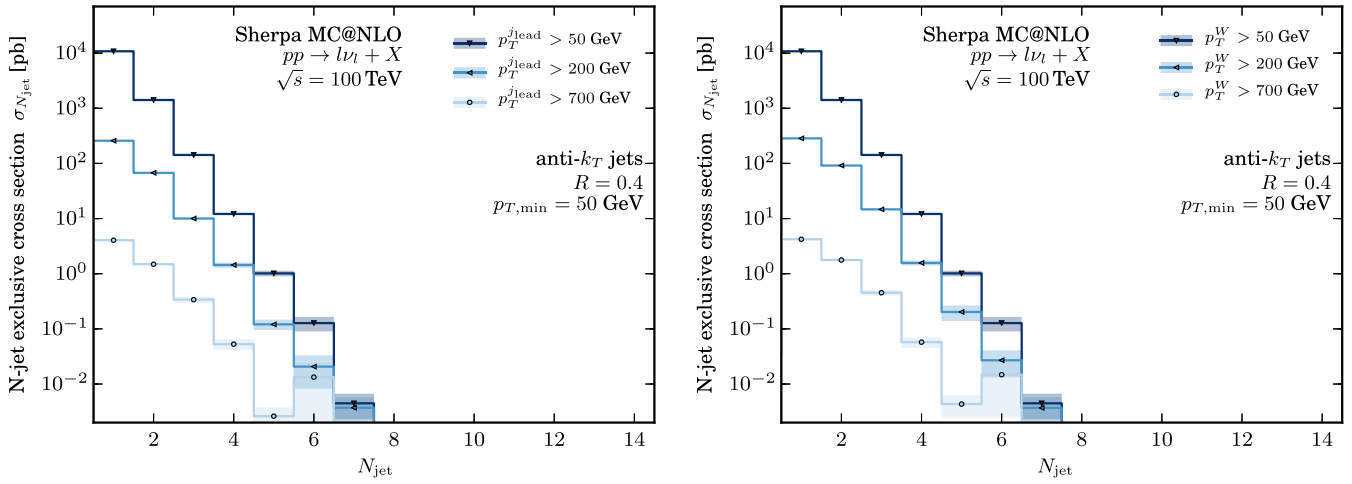

FIG. 7. The same as in Fig. 6, but with multijet merging disabled.

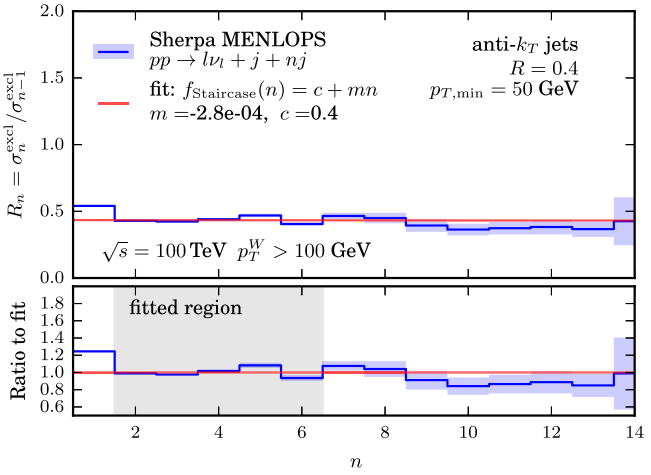

FIG. 8. Exclusive jet multiplicity ratios in W production for a democratic jet selection, i.e. applying a universal jet cut of $p_{T,\min} = 50$ GeV and requiring $p_{T,W} > 100$ GeV. As the fit function the staircase hypothesis given in Eq. (2.2) has been used.

scenarios have been considered, namely $p_T^{j_{\text{lead}}} > 500$ GeV and $p_T^W > 500$ GeV while $p_{T,\min} = 50$ GeV is still required. The results for the fits of the Poisson hypothesis in the range $1 \le n \le 4$ illustrate the significantly larger average jet number $\bar{n} = 2.7$ in the first case vs $\bar{n} = 1.1$ in the latter case. The constant offset parameters c are determined as $c = 0.1$ and $c = 0.4$, respectively. The extrapolations of both fits yield a good description of the simulated data up to very high jet counts.

To illustrate the universality of jet scaling patterns, Fig. 10 compiles the exclusive jet multiplicity ratios for a variety of processes, including pure jets, $\gamma +$ jets, $t\bar{t} +$ jets and $W/Z +$ jets. The predictions are based on dedicated n-jet tree-level matrix element calculations, without invoking parton showers. Democratic jet selection cuts are applied, requiring $p_{T,j} > 50$ GeV in all processes. In addition, the photon production processes are regulated by the selection criteria $p_{T,\gamma} > 50$ GeV and $R_{j,\gamma} > 0.4$, where $R_{j,\gamma}$ is the $\eta - \phi$ distance between all jets and the photon.

There are a few remarkable aspects to note here. Apparently, for the pure jets and $W +$ jets processes these LO rate estimates nicely reproduce the staircase scaling parameters found in the matrix-element plus parton-shower samples for the analogous jet-selection cuts, c.f. Fig. 5 (upper left panel) and Fig. 8. This is supported by the fact that for exact staircase scaling the cross-section ratios for subsequent jet multiplicities are identical for exclusive and inclusive cross sections [58]:

$$\frac{\sigma_{n+1}^{\text{excl}}}{\sigma_n^{\text{excl}}} = \frac{\sigma_{n+1}^{\text{incl}}}{\sigma_n^{\text{incl}}} = R = \text{const.} \tag{2.4}$$

Also note that the ratios of the three vector-boson production processes, $W/Z/\gamma +$ jets, are basically the same, illustrating the fact that the actual gauge-boson mass does not yield a big imprint on the jet-production probabilities. The production of a pair of top quarks, however, induces a large upper scale for subsequent jet emission. Correspondingly, the jet rates for the first few emissions are sizable, resulting in ratios $R_{(n+1)/n} > 0.5$, indicating that a pure leading-order approximation is inappropriate.

To summarize this section: it is possible to fit jet multiplicities n reasonably well up to values of $n = 15$ or even higher, using results for much lower n. The underlying fits are based on the theoretical hypothesis of simple scaling patterns, namely staircase and Poissonian scaling. These extrapolations allow meaningful predictions for very high jet-multiplicity bins that will be populated by a variety of production processes at FCC energies.

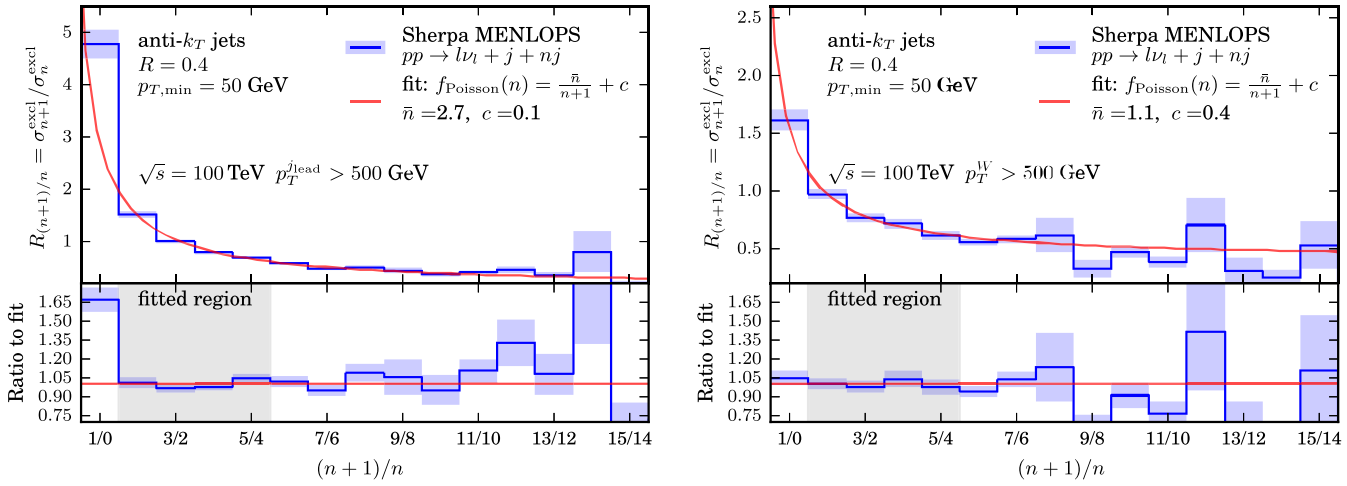

FIG. 9. Exclusive jet multiplicity ratios in W production with hierarchical event selection cuts. In the left panel, a cut on the leading jet of $p_T^{j_{\text{lead}}} > 500$ GeV is applied, whereas in the right panel, the cut on the W transverse momentum is $p_T^W > 500$ GeV. As the fit function the Poisson hypothesis given in Eq. (2.3) has been used.

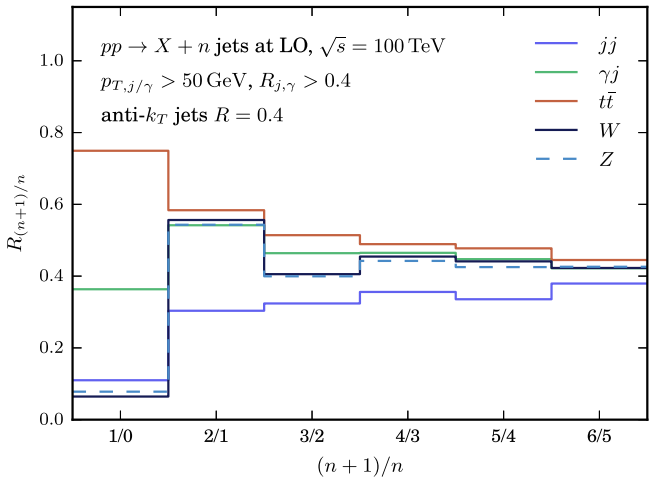

FIG. 10. The jet multiplicity ratio $R_{(n+1)/n}$ for several processes calculated at LO for each final-state multiplicity. Note that the index n counts jets associated to the core process listed in the legend.

The methods discussed enable the use of techniques that discriminate new physics signals and QCD backgrounds based on the shape of the jet-multiplicity distribution.

III. JET SUBSTRUCTURE AND BOOSTED TOPOLOGIES AT HIGH TRANSVERSE MOMENTUM

The enormous collision energies at a 100 TeV hadron-collider machine not only allow for the production of final states with a large number of well-isolated QCD jets, but furthermore enable the creation of heavy resonances that subsequently decay. Even for massive particles, the fraction of events where these states are produced with large transverse boosts can become quite sizable. This becomes even more apparent when these particles originate from the decay of heavy new particles in the multi-TeV mass range. Identifying such production processes by reconstructing the decay products, in particular for hadronic decays, provides a severe challenge for the detector designs. The separation of very collimated event substructures requires a fine granularity of the calorimeters to be supplemented by the use of particle-tracking information, known as particle-flow techniques [71,72]. Certainly, the methods currently used at the LHC for tagging such processes, e.g. for boosted hadronic top quarks or Higgs bosons, will need to be revised and probably overhauled [73–76].

The usage of large-area QCD jets, "fat jets," which are assumed to contain the hadronic decay products of the produced resonance and the majority of the associated QCD radiation, is prototypical for substructure analyses. At the LHC, typical radii for such fat jets are of the order of $R \approx 1$, but it is clear that larger boosts—larger transverse momenta—will necessitate smaller radii, usually of the order of $R \approx 2M/p_T$, where M is the mass of the heavy particle. Assuming a top quark with a transverse momentum of around 3.5 TeV, originating from a hypothetical 7 TeV resonance, the resulting fat jet will have a radius of around $R \approx 0.1$ only. This clearly poses a considerable challenge for the granularity of future detectors. However, assuming suitable fat jets have been identified, specialized tagging methods are used, which analyze their substructure. This is achieved through, for example, reclustering the large-jet constituents into smaller subjets, or in terms of jet-shape-like measures. For reviews of the currently available techniques see Refs. [77–80]. Vital for all these approaches is a good theoretical understanding of both the backgrounds from pure QCD jets and the radiation pattern of the heavy resonance and its decay products. The complexity of the tagging methods used often allows for a comparison of the response from different Monte Carlo generators only. However, there is a lot of activity to develop predictive analytical techniques; see for instance Refs. [81–86].

In the following the focus will be on a rather coarse feature of large-area QCD jets at high transverse momentum, namely the mean number of small-R subjets $\langle n_{\text{subjets}} \rangle$ found inside fat jets. Results will be finally compared to the corresponding observable for highly boosted hadronic decays of top quarks and W bosons. The number of subjets found inside a larger jet is expected to carry information on the QCD color charge of the jet initiating particle. Broadly speaking, at lowest order one expects the scaling behavior $\langle n_{\text{subjets}} \rangle \propto C_A$ for color octets and $\langle n_{\text{subjets}} \rangle \propto C_F$ for color triplets. Based on such considerations one can attempt to discriminate gluon from quark jets [87,88], i.e. assign a corresponding likelihood based on the jet-internal QCD activity. For hadronic decays of color singlets, a reduced and more collimated QCD radiation can be expected, resulting in a smaller number of subjets to be found.

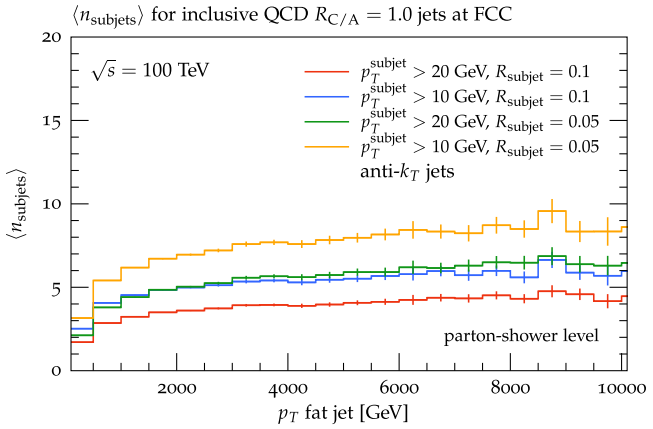

FIG. 11. Average number of subjets inside Cambridge-Aachen jets of $R = 1.0$ in inclusive QCD-jet production. Subjets are reconstructed using the anti-k_T jet finder with $R_{\text{subjet}} = 0.05$, 0.1 and $p_T^{\text{subjet}} > 10$, 20 GeV. Results are presented at parton level.

Considering the physics case of highly boosted hadronic decays, rather small radii R_{subjet} need to be considered.

To set the stage, Fig. 11 compiles the expectation for the average number of anti-k_T subjets found inside large-area Cambridge-Aachen jets of size $R_{C/A} = 1.0$ [30] as a function of the fat-jet transverse momentum. This potentially allows contact to be made with LHC results in the future. Results are obtained from a SHERPA dijet simulation, invoking parton showers but neglecting any nonperturbative corrections, like parton-to-hadron fragmentation and the underlying event. While the results shown here were obtained from the parton shower based on Catani-Seymour dipoles [43], they have carefully been checked and confirmed using the independent DIRE shower implementation [89] in SHERPA.

In all results, two benchmark values for R_{subjet} are considered, $R_{\text{subjet}} = 0.05$ and 0.1. Furthermore, two threshold values for the subjet transverse momentum are used, namely $p_T^{\text{subjet}} > 20$, 10 GeV. Clearly, $\langle n_{\text{subjets}} \rangle$ grows with smaller R_{subjet} and p_T^{subjet} cut. For the mixture of quark and gluon jets given by the LO matrix elements in this calculational setup, a mean number of subjets of $\langle n_{\text{subjets}} \rangle \approx 5$ for $p_T^{\text{fat}} = 3.5$ TeV, $p_T^{\text{subjet}} > 10$ GeV and $R_{\text{subjet}} = 0.1$ is found. In the following, the LO matrix elements for quark and gluon production will be considered separately, in order to contrast them individually. However, for all considered parameter choices the slope of the $\langle n_{\text{subjets}} \rangle$ distributions levels off for large values of the fat-jet p_T, corresponding to very collimated jet-energy profiles. In this regime of large p_T, the actual jet inside the fat-jet area becomes comparable in size to the subjet size, and it becomes increasingly harder to push more subjets into the jet.

Using very small R_{subjet} and p_T^{subjet} is not only an experimental challenge for reconstruction algorithms but it also induces large logarithms that need to be resummed in order to obtain a reliable prediction. Both of the jet algorithms considered here fall into the family of generalized longitudinally invariant k_t algorithms. They all rely on a distance measure between all pairs of particles i and j given by

$$d_{ij} = \min\left(p_{T,i}^{2p}, p_{T,j}^{2p}\right) \frac{(\Delta R_{ij})^2}{R^2} \tag{3.1}$$

and a separation between all particles and the beam direction,

$$d_{iB} = p_{T,i}^{2p} \tag{3.2}$$

where $p_{T,i}$ is the transverse momentum of particle i and $(\Delta R_{ij})^2 = (y_i - y_j)^2 + (\phi_i - \phi_j)^2$, where y_i denotes the rapidity and ϕ_i is the azimuth angle of the particle i. The parameter p determines the actual jet algorithm. The choices $p = 1$, 0, -1 correspond to the k_T [90], Cambridge-Aachen [91] and anti-k_T [29] jet finder, respectively. R corresponds to the jet-radius parameter already mentioned above. For this class of jet algorithms there are predictions resummed for small R to all orders of $(\alpha_s \log R^2)$ [57,92], and for small R and small transverse-momentum threshold $p_{\text{T,min}}$ of $(\alpha_s \log R^2 \log(p_T/p_{\text{T,min}}))$ to double and next-to-double logarithmic approximations [55,88]. In particular, Ref. [55] derived resummed predictions for jet rates and the mean number of jets to double-logarithmic (DLA) and next-to-double-logarithmic approximations (NDLA), accounting for effects of the running of the strong coupling. It should be noted that at this level of accuracy the results are independent of the parameter p that distinguishes the jet algorithms.

In Fig. 12, resummed predictions to DLA and NDLA accuracy including the effect of the running of α_s to one-loop order are presented for $\langle n_{\text{subjets}} \rangle$ for both light-quark and gluon-initiated jets of size $R = 1.0$. It can be observed

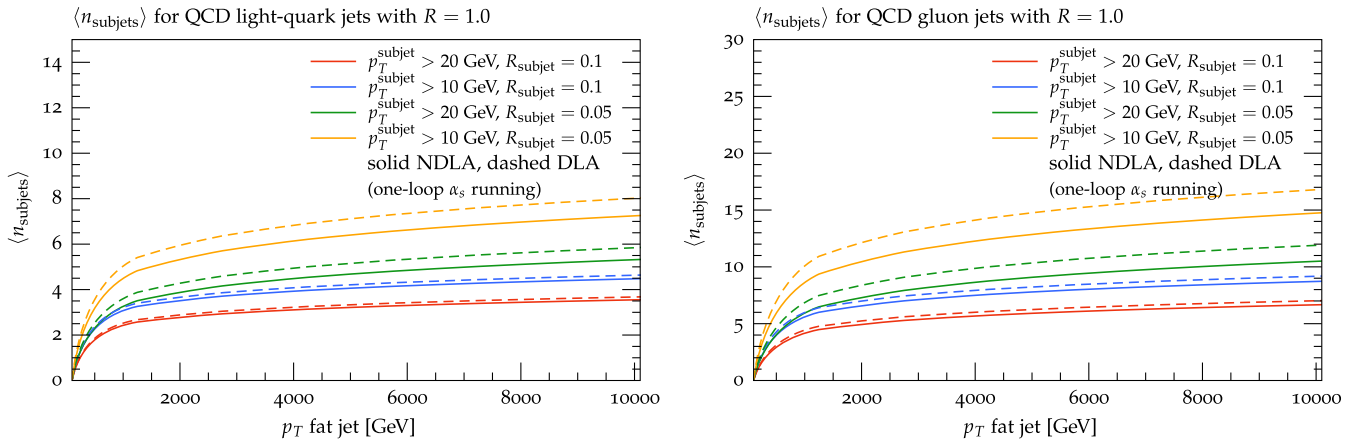

FIG. 12. NDLA (solid) and DLA (dashed) predictions for the mean number of subjets inside $R = 1.0$ light-quark (left panel) and gluon (right panel) initiated jets for different choices of p_T^{subjet} and R_{subjet}.

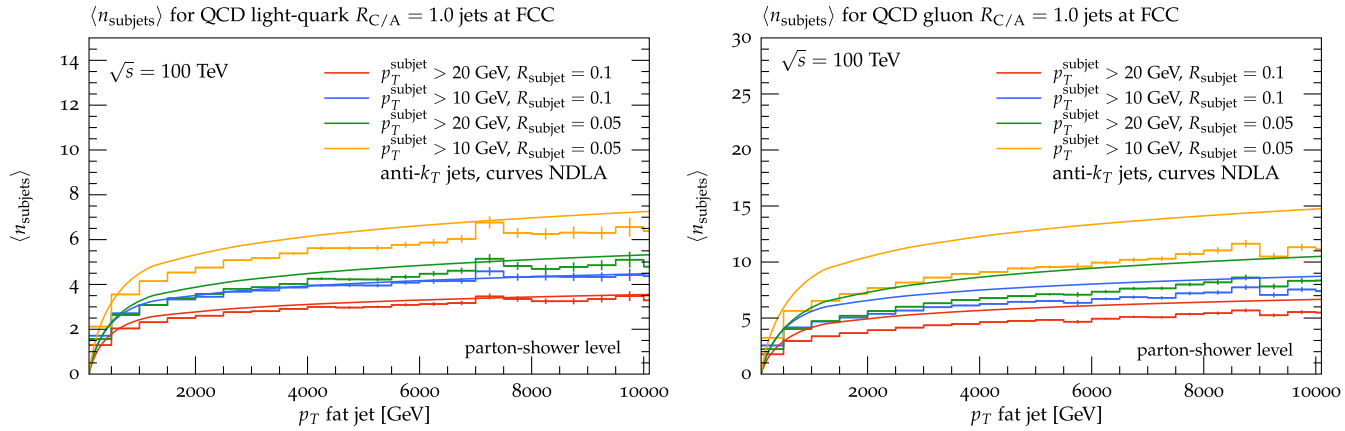

FIG. 13. Average number of subjets inside $R = 1.0$ light-quark (left panel) and gluon (right panel) initiated jets. A SHERPA parton-shower simulation (histograms) is compared to corresponding NDLA resummed predictions (solid curves) for different choices of p_T^{subjet} and R_{subjet}.

that for all combinations of R_{subjet} and $p_{T,\text{min}}^{\text{subjet}}$ gluons induce a larger mean number of subjets than quarks, as naively expected from the color charges. The NDLA corrections are most sizable for $R_{\text{subjet}} = 0.05$, where they reduce the DLA prediction significantly.

In Fig. 13 the comparison of the $\langle n_{\text{subjets}} \rangle$ distribution for a SHERPA parton-shower simulation and the corresponding NDLA prediction for quark- and gluon-initiated jets is presented. For the shower simulation, the processes $pp \to q\bar{q}$ and $pp \to gg$ have been considered, respectively. Given the large jet transverse momenta investigated here, initial-state parton-shower effects are rather suppressed and a comparison to the pure final-state evolution hypothesis of the resummed calculation is applicable.[3] For the case of quark-initiated jets, the resummed predictions agree well with the parton-shower results, and the dependence on the fat-jet transverse momentum is very well reproduced. For $R_{\text{subjet}} = 0.05$ the resummation overshoots the shower prediction by about 10%. When comparing the results for gluon jets, somewhat larger deviations are observed. Once again the parton shower nicely reproduces the shape of the resummed prediction. However, the NDLA results overshoot the Monte Carlo simulation by about 20% for $R_{\text{subjet}} = 0.1$ and 25% when $R_{\text{subjet}} = 0.05$. It has been observed before that resummed predictions for gluon jets tend to produce larger deviations from shower generators [88] and that the latter predict somewhat lower rates, in particular when considering small jet radii. Since in general gluons radiate more than quarks, they are thus more sensitive to missing higher-order terms. For R_{subjet} values as small as 0.1 or even 0.05 the analytic resummation of terms like $(\alpha_s \log(1/R_{\text{subjet}}^2))^n$ to all orders [57] or jet-clustering logarithms as discussed in Ref. [93] might need to be considered. Furthermore, explicit calculations of the next-to-NDLA contributions to k_T jet rates turn out to give sizable corrections and improve the agreement with parton-shower simulations.[4]

Overall, one can conclude that parton-shower predictions for the mean number of subjets in large-area jets give reliable results that are in reasonable agreement with analytical estimates from resummed calculations. However, in particular for the case of gluon jets higher-logarithmic contributions seem to yield sizable corrections. However, for subjet radii not too small the techniques presented allow realistic perturbative predictions to be made for very large jet transverse momenta and rather small subjet p_T thresholds. Certainly, for a dedicated comparison against data, non-perturbative corrections from hadronization and the underlying event need to be included. However, these are largely independent of the flavor of the particle that seeds the jet evolution and thus will not critically change the above picture. Instead, apart from slightly washing out some of the differences between quark and gluon jets, only a modest offset in the mean number subjets is expected.

The observable at hand, $\langle n_{\text{subjets}} \rangle$ as a function of the transverse momentum of a large-area jet, will now be considered as a discriminator for QCD jets and hadronic decays of heavy particles. In Fig. 14, a comparison of the mean number of subjets found inside Cambridge-Aachen jets of $R = 1.0$ containing the hadronic decay products of top-quarks, W-bosons and light-quark QCD jets is presented. In the analysis of the top-quark and W-boson decays, the reconstructed fat jet that is closest to the direction of the actual resonance is analyzed. The quark-jet distribution is obtained from the analysis of $pp \to q\bar{q}$

[3]This hypothesis has explicitly been checked and confirmed by switching off initial-state splittings in the SHERPA parton shower.

[4]Private communication with Bryan Webber based on unpublished results.

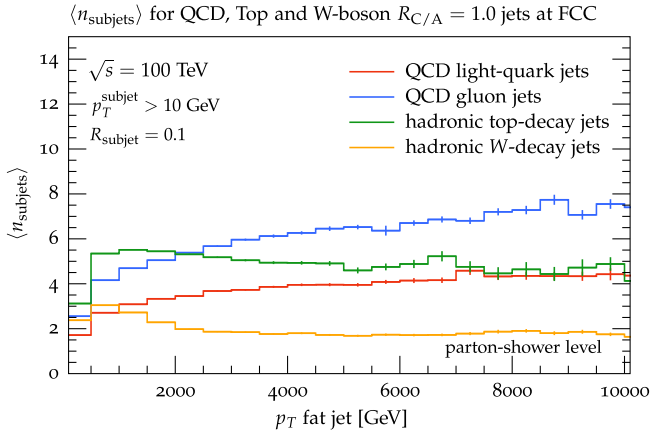

FIG. 14. Average number of subjets inside Cambridge-Aachen jets of $R = 1.0$ originating from hadronic top-quark and W-boson decays, and QCD quark-jet production. Subjets are reconstructed using the anti-k_T jet finder with $R_{\text{subjet}} = 0.1$ and $p_T^{\text{subjet}} > 10\,\text{GeV}$. Results are presented at parton level.

events. For R_{subjet} and p_T^{subjet} the values 0.1 and 10 GeV are considered, respectively.

Most notably, jets containing the decay jets of boosted $W \to q\bar{q}'$ decays feature a rather small number of subjets. This is related to the color-singlet nature of the W boson. Its decay jets are very collimated at high transverse momentum, with no color connection to the rest of the event, which characterizes the quark or gluon jets. This results in a rather constant expectation of just two subjets for $p_T^{\text{fat}} > 2$ TeV. At $p_T^{\text{fat}} \approx 1$ TeV three subjets are resolved on average, corresponding to the emission of one additional jet from the two decay partons. This prominent feature makes it easily possible to distinguish hadronic W-boson decays, or similarly Higgs-boson decays, from QCD jets.

The identification of top-quark decays based on $\langle n_{\text{subjets}} \rangle$ seems much harder. The distribution peaks around $p_T^{\text{fat}} \approx 1$ TeV with a value of $\langle n_{\text{subjets}} \rangle \approx 5.5$. This is significantly higher than what is observed for light-quark jets and even for gluon jets, and it is due to the hadronic decays assumed for the tops, i.e. $t \to bW^+ \to bq\bar{q}'$, which yield three jets—two more than the original quark. With increasing transverse momentum the top-jet distribution approaches the light-quark result, reflecting the fact that beyond $p_T^{\text{fat}} \approx 4$ TeV the decay products are extremely collimated and basically radiate with their combined color charge C_F as light-quark jets do. To illustrate this fact Fig. 15 compiles the $\langle n_{\text{subjets}} \rangle$ distribution for stable (undecayed) top quarks and bottom quarks. Three values of p_T^{subjet} are considered—5, 10 and 20 GeV—while R_{subjet} is fixed to 0.1. Mass effects, namely the shielding of collinear singularities, yield a suppression of radiation off top quarks up to p_T values of 4 TeV. The radiation off bottom quarks at high transverse momenta as considered here is compatible with the light-quark distributions presented in Fig. 13.

It can be concluded that at FCC collision energies the identification of very boosted hadronic decays becomes extremely challenging. The observable presented here, i.e. $\langle n_{\text{subjets}} \rangle$ of large-area jets, provides sensitivity to the QCD color charge of the jet-initiating particle—either a QCD parton or a heavy resonance. For QCD quark and gluon jets the results obtained from parton-shower simulations are in reasonable agreement with predictions from all-orders resummation calculations at NDLA accuracy.

IV. LOOP-INDUCED PROCESSES AT 100 TEV

A. Finite top mass effects in gluon fusion Higgs production

At a 100 TeV hadron-collider machine, the dominant production mechanism for a Standard-Model Higgs boson proceeds through top-quark loops that mediate an

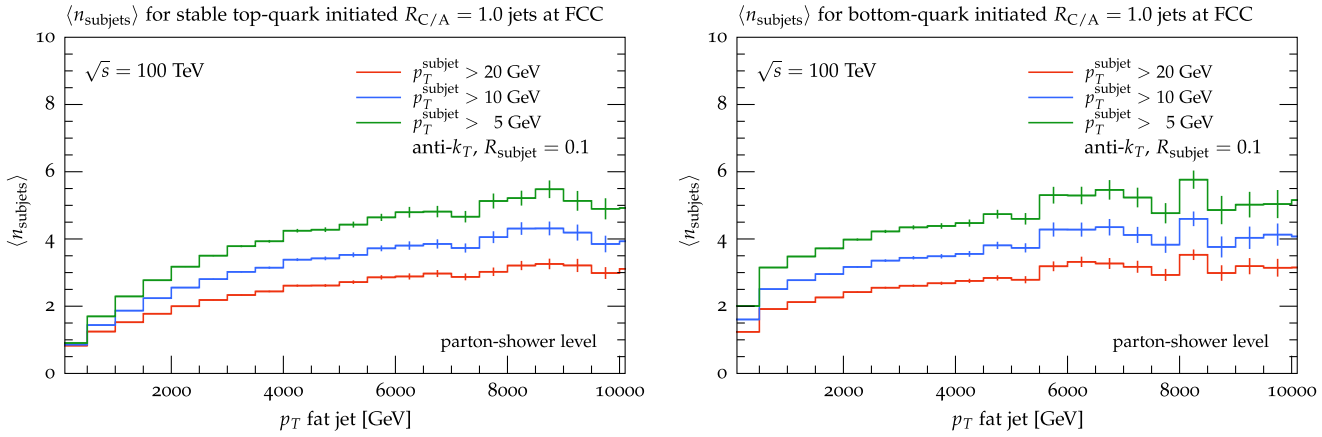

FIG. 15. Average number of subjets inside Cambridge-Aachen jets of $R = 1.0$ originating from stable top-quark and bottom-quark production. Subjets are reconstructed using the anti-k_T jet finder with $R_{\text{subjet}} = 0.1$ and $p_T^{\text{subjet}} > 5, 10, 20$ GeV. Results are presented at parton level.

interaction between gluons and the Higgs boson. The increased calculational complexity due to the presence of this loop, already at leading order, is commonly reduced by using the Higgs effective field theory (HEFT) approximation. In this approach, the top-quark loop-mediated couplings between gluons and the Higgs boson are approximated in terms of direct tree-level couplings that can be derived from the effective Lagrangian

$$\mathcal{L}_{\mathrm{HEFT}} = \frac{\alpha_s}{12\pi} G^a_{\mu\nu} G^{\mu\nu}_a \ln\left(1+\frac{H}{v}\right) \tag{4.1}$$

$$= \frac{\alpha_s}{12\pi} G^a_{\mu\nu} G^{\mu\nu}_a \left[\left(\frac{H}{v}\right) - \frac{1}{2}\left(\frac{H}{v}\right)^2 + \frac{1}{3}\left(\frac{H}{v}\right)^3 - \ldots\right], \tag{4.2}$$

with the gluon field-strength tensor $G_{\mu\nu}$ and the Higgs field H. This Lagrangian gives rise to tree-level couplings that can be understood as the infinite top-mass limit, i.e. $m_t \to \infty$, of the respective loop-induced SM couplings between gluons and the Higgs boson.

For the calculation of the inclusive total cross section at LHC energies, the application of the HEFT approximation is well motivated since finite top-quark mass corrections turn out to be moderate [94–99]. This applies both to inclusive Higgs production and to Higgs production in association with one or two jets [100,101]. However, the tail of the Higgs-boson transverse momentum distributions is only poorly modeled in HEFT [102,103], with the infinite top-mass approximation overshooting the m_t-exact result. The purpose of this section is to quantify such effects at a 100 TeV hadron collider.

The results presented in this section are obtained from leading-order calculations of inclusive Higgs production processes in association with one, two, and three jets, including top-mass effects, based on one-loop matrix elements from OPENLOOPS [17,104]. For the evaluation of scalar and tensor integrals the COLLIER library [18,105] and CUTTOOLS [13] is employed. A full NLO QCD calculation in the HEFT framework, but including top-mass effects in the approximation of Ref. [100] is feasible with SHERPA but not necessary in order to capture the characteristics of the mass corrections, as they have proven to factorize to a good approximation from the NLO QCD corrections [106]. For the purpose of studying the top-mass effects in the hard scattering process, parton-shower effects are not considered here.

In Fig. 16 the transverse-momentum distribution of Higgs production at 13 and 100 TeV with up to three jets is presented. From the ratio plots in the lower panels of Fig. 16 it is evident that the relative size of the finite top-mass corrections to the p_T distributions exhibit the same universal suppression pattern for all jet multiplicities. This is in accordance with similar findings in Refs. [100,107] where the production of up to two associated jets at LHC energies has been studied. When comparing the results for collider energies of 13 and 100 TeV, the similarity of the relative size of the corrections is quite remarkable. Considering the increase in partonic energy that is available at 100 TeV, one could have expected that for a given value of Higgs p_T, the mean partonic center-of-mass energy would be higher, thus giving rise to larger discrepancies between the HEFT calculation and the m_t-exact

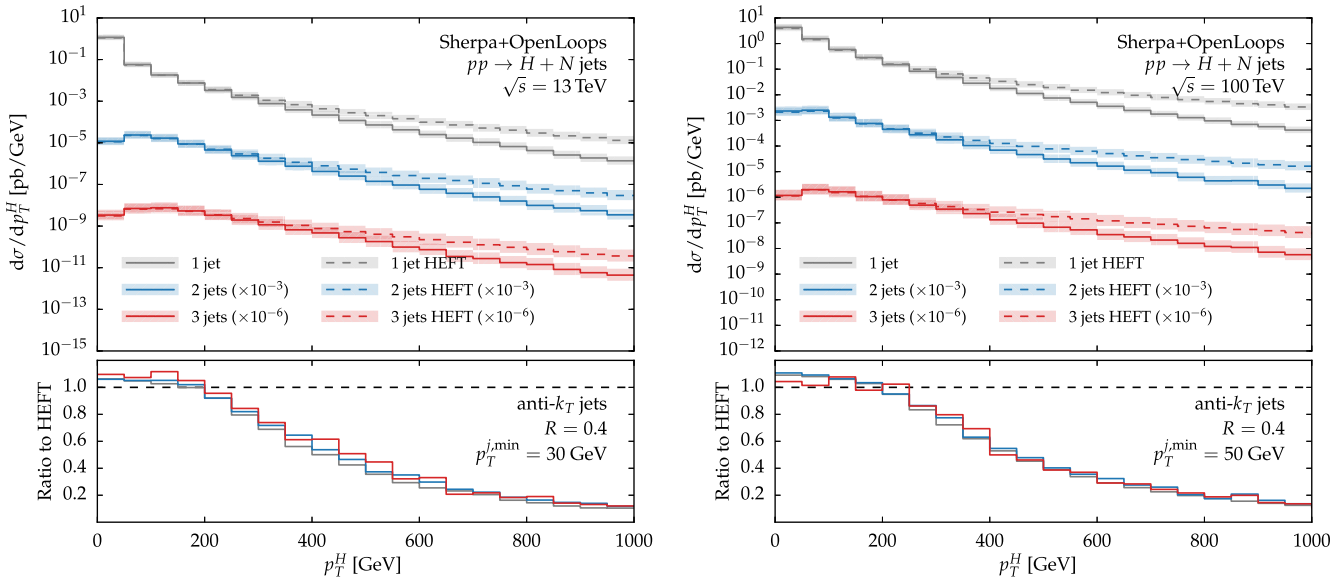

FIG. 16. Higgs transverse-momentum distributions in gluon-fusion Higgs production in association with up to three anti-k_T jets with $R = 0.4$ and $p_{T,j} > 50$ GeV. The distributions are obtained from leading-order calculations of the respective process. Results for the infinite top mass (HEFT) and the m_t-exact calculation are shown. The lower panels show the ratio of the full m_t-exact result and the HEFT approximation.

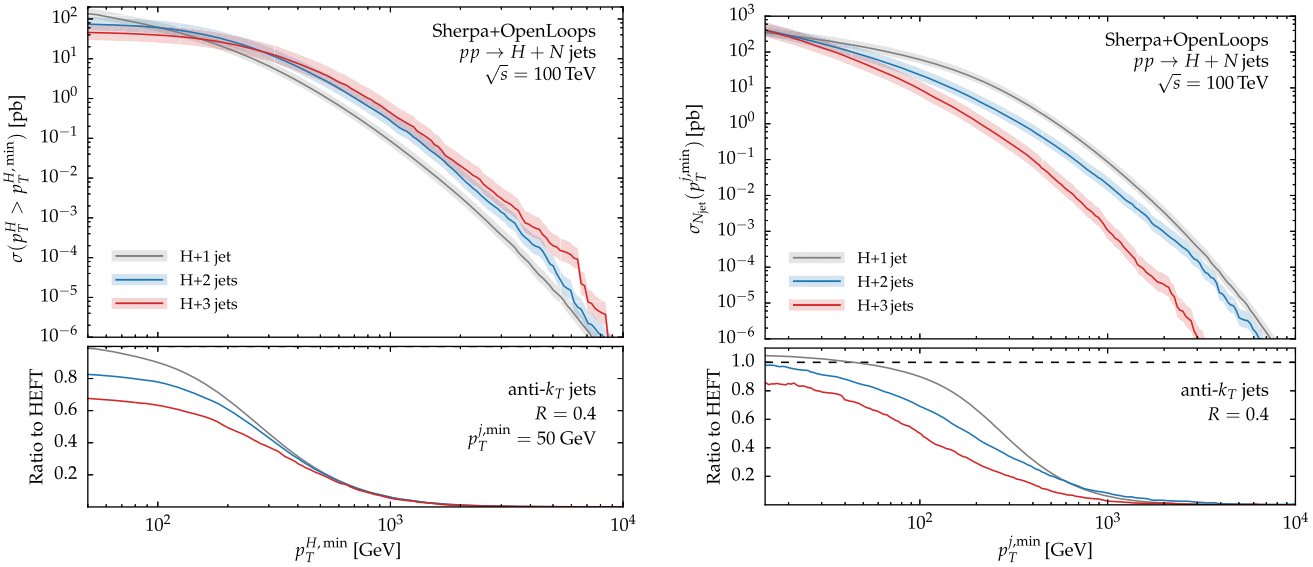

FIG. 17. Fixed-order cross sections for Higgs production in association with up to three jets as a function of a minimum Higgs p_T cut (left panel) and as a function of the minimum jet p_T (right panel) with finite top-mass effects taken into account. The lower panels show the ratios to the respective HEFT predictions and quantify the finite top-mass corrections.

calculation. This is, however, not the case, even for three-jet final states, where the jets can in principle carry away large amounts of additional energy.

This effect can indeed be observed when considering cumulative distributions, as exemplified in Fig. 17. The total cross section receives large finite top-mass corrections at 100 TeV when applying a minimum transverse-momentum cut on the Higgs. This is due to the fact that the tail of the Higgs transverse-momentum spectrum extends further into the high-energy regime, where finite top-mass effects are large. The effect is already substantial for a cut of $p_T^H > 50$ GeV, where the HEFT result overshoots the m_t-exact result by more than 50% in the three-jet case. The same effect can be observed in the n-jet inclusive cross sections that are displayed in the right panel of Fig. 17 as a function of the minimum jet transverse momentum. Even for moderate cuts on the jet transverse momenta around $p_T^{\rm jet} = 50$ GeV, large corrections of the order of -30% are observed, indicating a poor description even of very inclusive observables in three-jet final states. Table II illustrates this further with the leading-order cross sections for all three jet multiplicities at $p_T^{j,\min} = 50$ GeV. Higher jet multiplicities are particularly relevant for the description of the Higgs p_T spectrum above 200 GeV. As demonstrated in the left panel of Fig. 17, the three-jet contributions exceed both the one- and the two-jet contributions in magnitude in this boosted regime. This feature of the transverse-momentum distribution is however not specific to FCC energies but can be observed at the LHC as well [108].

TABLE II. Leading-order inclusive production cross sections at the FCC for H-boson production in association with $n = 0$, 1, 2, 3 jets based on the m_t-exact calculation (SM) and the HEFT approximation. Jets are reconstructed using the anti-k_T algorithm with $R = 0.4$ and $p_T^{j,\min} = 50$ GeV.

	H	Hj	Hj^2	Hj^3
SM	229 pb	137 pb	79 pb	47 pb
HEFT	215 pb	138 pb	94 pb	68 pb

It can be concluded that in contrast to the situation at the LHC, finite top-mass effects are sizable at 100 TeV even when considering inclusive jet cross sections with moderate cuts on the jet transverse momentum. It should furthermore be noted, that at a future 100 TeV hadron collider the event rates for Higgs-boson production in association with TeV-scale jets easily exceed several femtobarns. In this kinematic regime, the HEFT approximation completely fails and finite top-mass effects must be taken into account in order to obtain meaningful predictions.

For completeness, we also compare the infinite top-mass approximation to the di-Higgs production with the m_t-exact SM result. It is well established that for this process even the fully inclusive cross section at the LHC is poorly approximated in the HEFT approximation [109]. We demonstrate this for FCC energies in Fig. 18, where we show the di-Higgs invariant mass spectrum. Even near threshold, the HEFT approximation fails to even remotely reproduce the shape of the invariant mass distribution. The same holds for the inclusive production cross sections quoted in Table III.

B. Loop-induced diboson processes

In contrast to single- and di-Higgs production, where loop-induced contributions are dominant, the production of other diboson final states is typically dominated by

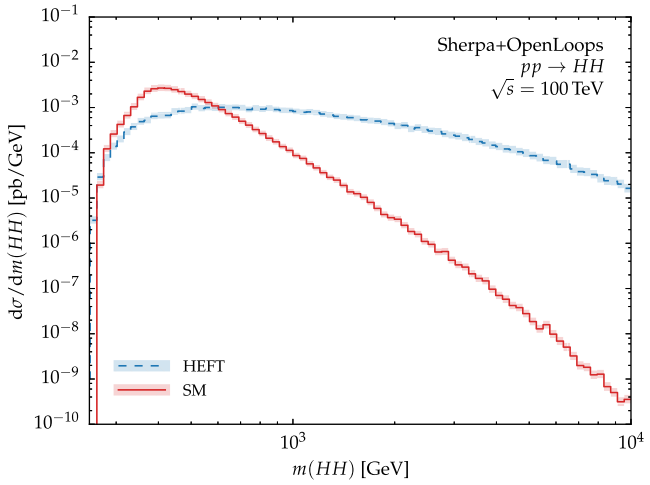

FIG. 18. Di-Higgs invariant-mass distributions as calculated in the infinite top-mass limit (HEFT) and with the exact top-mass dependence taken into account (SM) at leading order.

quark-induced partonic channels that proceed through tree-level diagrams at leading order. Loop-induced contributions with gluons in the initial state nonetheless often exist and contribute to the production. Despite being part of a next-to NLO (NNLO) QCD correction to the tree-induced process, their relative size for fairly inclusive LHC cross section energies can range from a few percent, in the case of the $pp \to WW \to l\bar{\nu}_l \bar{l}' \nu_{l'}$ process [110], to around 20% for $pp \to ZZ \to 4l^{\pm}$ [111], thus exceeding the naive expectation of $\alpha_s^2 \approx 1\%$. This is in part due to the large gluon luminosity in the Bjorken-x range probed by the process under consideration. At a 100 TeV collider, we expect this effect to be enhanced, since, for a final state of given mass, the x range probed will be shifted towards smaller values where the gluon PDFs dominate. Furthermore, corrections to Higgs processes which are mediated by heavy quark loops can feature additional threshold effects that increase their relative size even further [112]. As in the previous section, we employ the OPENLOOPS one-loop matrix element provider along with COLLIER and CUTTOOLS and calculate all loop-induced processes at leading order. We set the renormalization, factorization and parton shower starting scales to $\sqrt{\hat{s}}/2$ for all processes and take into account parton-shower effects.

As representatives for processes whose gluon-induced components proceed predominantly through loops of light-quark flavors, we consider W-pair production, Z-pair production and photon-associated Z-boson production. We use matrix elements for the full leptonic final states with all interference and off-shell effects taken into account. For W-pair production, we consider the $e^-\bar{\nu}_e\mu^+\nu_\mu$ final state, while for the ZZ process we generate $pp \to e^-e^+\mu^-\mu^+$. For photon-associated Z production, we consider the $e^+e^-\gamma$ final state. All leptons are required to pass a minimum transverse momentum cut of 50 GeV. The photon is required to pass the same transverse-momentum cut. In addition, we require the photon to be well separated from the leptons with $\Delta R(\gamma, e^{\pm}) > 0.4$. Invariant-mass cuts on lepton pairs are applied in such a way as to ensure that the intermediate vector bosons are near their mass shell with $|m_V - m(ll)| < 15$ GeV. The quark-induced processes that proceed through tree-level diagrams at leading order are calculated at NLO QCD accuracy with the exception of the $e^+e^-\gamma$ process, which is calculated only at leading order.

In Fig. 19 we show the diboson invariant-mass distributions and the single-boson transverse-momentum spectra for the three aforementioned processes. Individual curves for the gluon-induced one-loop processes and for the quark-induced tree-level processes illustrate the relative size of the loop-induced components. With the set of cuts applied, we observe that the relative size of the loop-induced contributions remains moderate. For W-pair production, the corrections remain at the percent level, while the $pp \to ZZ$ process receives corrections of the order of 15% from gluon-induced channels. In the $Z\gamma$ process, these channels still contribute a substantial, yet somewhat smaller correction as in the case of ZZ production. Due to the different structure of contributing Feynman diagrams and because of the differences in the underlying PDFs, there are however significant shape differences when comparing loop-induced processes with their respective tree-induced counterparts.

In addition to the processes above we also consider Z-associated Higgs-boson production. In contrast to the previously mentioned processes, the gluon-induced component of the ZH process is mediated by loops of heavy quarks. This is manifest in the presence of a top-pair threshold which is clearly visible in the ZH invariant mass distribution shown in the left panel of Fig. 20. Differentially, the gluon-induced corrections are strongly enhanced with respect to the tree-like contributions for invariant-mass values around $2m_t$. The magnitudes of both contributions are in fact of the same order in this region. This effect can be observed already at LHC energies to some extent [112]. With the loop-induced contributions being comparable to the tree-like contributions in terms of magnitude, it is, however, much more pronounced at FCC energies.

It should be stressed here that the results for loop-induced processes presented so far are only leading-order accurate. NLO corrections to the corresponding partonic channels are expected to be very large as in the case of

TABLE III. Leading-order inclusive production cross sections for Higgs pair production at the FCC based on the m_t-exact calculation (SM) and the HEFT approximation.

	SM	HEFT
$\sigma(gg \to HH)$	0.74 pb	2.1 pb

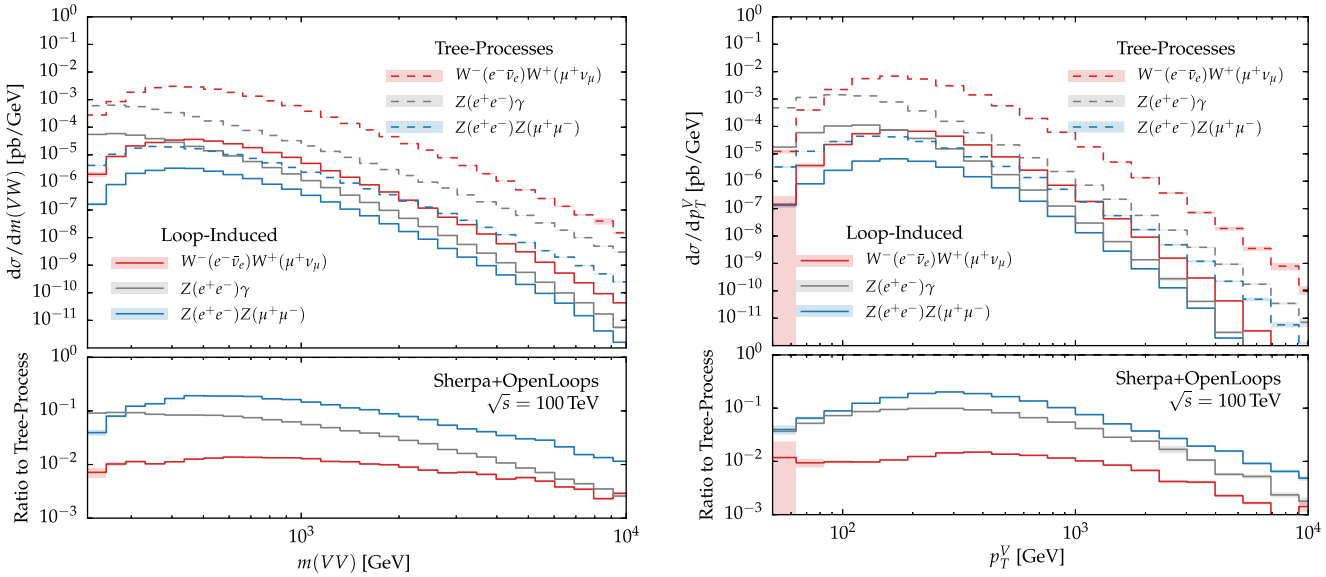

FIG. 19. Left panel: Invariant mass of the vector-boson pairs in W^+W^- and ZZ production. Right panel: Transverse-momentum distribution of the W^- and the Z decaying to electrons. The solid curves show loop-induced contributions while the dashed curves represent tree-like contributions. The lower panel shows the ratio of the loop-induced contributions to the tree-level contributions.

single-Higgs production in gluon fusion. In most cases, NLO corrections have not been calculated for loop-induced processes due to the considerable complexity of the required two-loop amplitudes. Critical features of NLO real corrections to such processes can, however, be captured by means of leading-order multijet merging with SHERPA [112,113]. For this purpose, QCD real-emission matrix elements are combined with the core process and the parton shower in such a way as to correct hard parton-shower emissions with appropriate matrix elements. For these hard emissions, the fixed-order matrix-element accuracy is thereby ensured while maintaining the logarithmic accuracy of the parton shower as well. Given the increased energy available to produce additional hard QCD radiation (cf. Sec. II), an accurate description of the corresponding event topologies is of utmost importance.

The effects of incorporating higher-multiplicity matrix elements are particularly notable when considering observables that are generated entirely by QCD corrections to the leading-order process. As examples, we consider

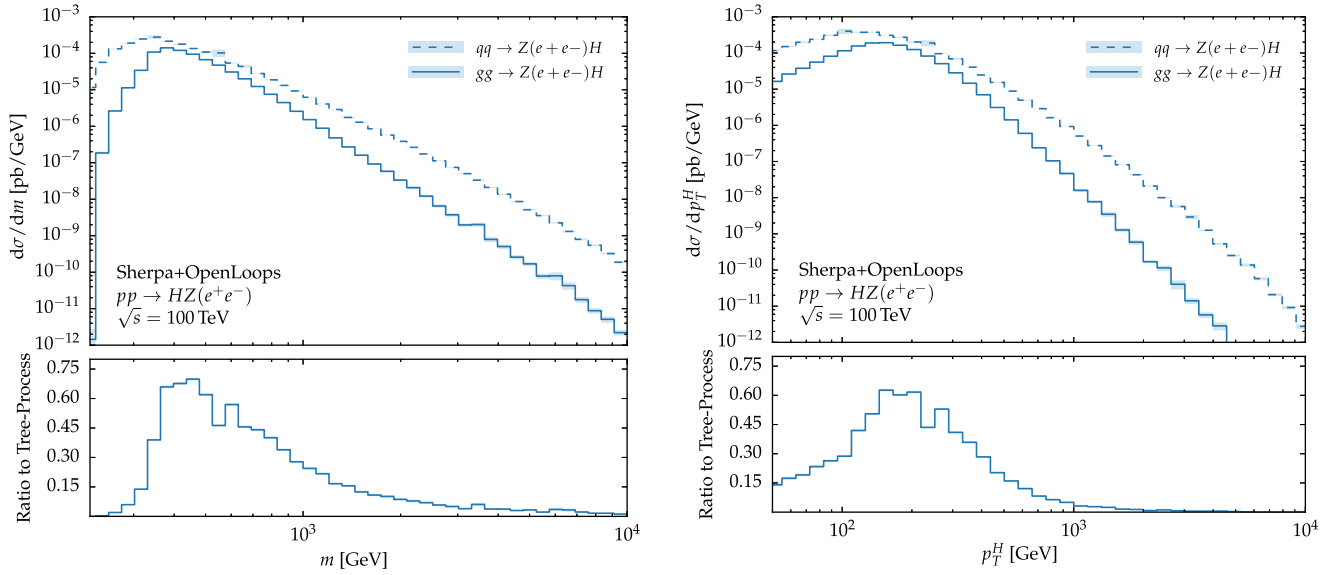

FIG. 20. Diboson invariant mass (left) and Higgs transverse momentum distribution (right) in Z-associated Higgs production. We show both the gluon-induced contributions (solid) and the quark-induced tree-like contributions as well as the ratio of the two (lower panels).

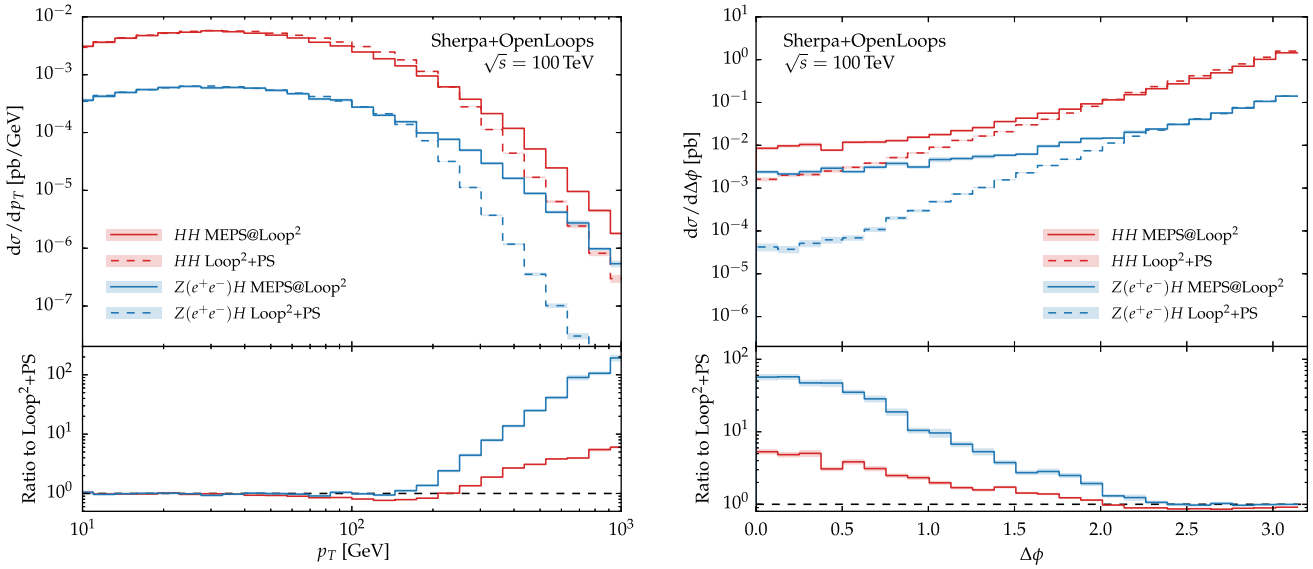

FIG. 21. Transverse momentum of the diboson final state (left) and azimuthal separation of the diboson pair (right) in Higgs-pair production and loop-induced Z-associated Higgs production. We show results obtained from a merged calculation (solid) and results as obtained from a pure parton-shower simulation (dashed) as well as the ratio of the two (lower panels).

loop-induced Higgs-pair production and Z-associated Higgs production and calculate the transverse-momentum distribution of the HH system and the ZH system, respectively. Figure 21 shows the corresponding results as obtained from a simulation based on the leading-order matrix element combined with a parton shower (Loop^2 + PS) in comparison to a merged calculation (MEPS@Loop^2). In the merged calculation, we take matrix elements with up to one extra jet in the final state into account. At leading order, the transverse momentum of the diboson system is zero, as required by momentum conservation. In the Loop^2 + PS simulation, the spectrum is therefore generated purely by the parton shower. For kinematic configurations that contribute in the tail of this distribution, the soft/collinear approximation inherent to a parton shower breaks down, and the corrections one observes when utilizing multijet-merging techniques are correspondingly large, as quantified in Fig. 21. Also shown in this figure is the azimuthal separation $\Delta\phi$ of the diboson pair. Similarly to the transverse-momentum spectrum of the diboson system, a nontrivial distribution is generated entirely though QCD real-emission corrections. Any configuration with $\Delta\phi \neq \pi$ requires additional radiation to be present in the final state giving rise to a decorrelation of the boson pair in the azimuthal plane. In regions far away from back-to-back configurations with $\Delta\phi = \pi$, one can observe large effects induced by the higher-multiplicity matrix elements.

Large merging effects can also be observed when considering observables that receive nontrivial contributions already from leading-order matrix elements. As an example, we show the Higgs transverse-momentum spectrum in Fig. 22 in Z-associated Higgs production. In this case, QCD real emission contributes an actual higher-order correction to the lowest-order result since the Higgs can recoil against the Z already in a Born-like kinematic configuration. Contrary to naive expectations, these corrections are substantial. In the tail of the distribution, the Loop^2 + PS result undershoots the spectrum by an order of magnitude. This indicates that, in this regime, the Higgs-boson recoils predominantly against a jet rather than

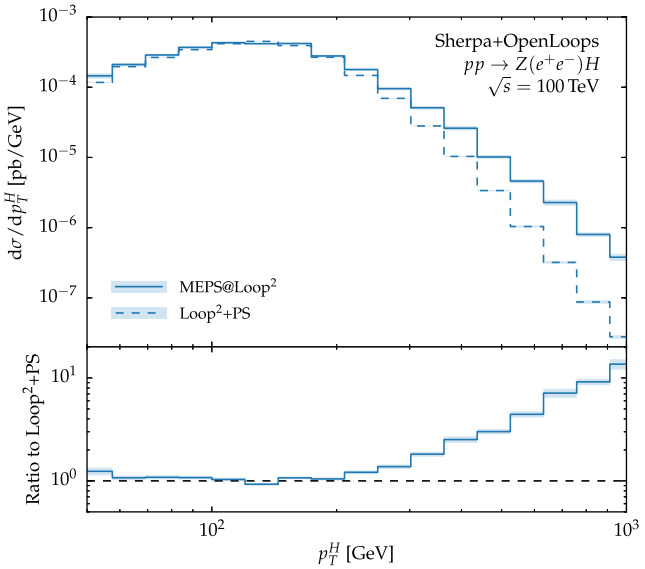

FIG. 22. Higgs transverse momentum distribution in loop-induced Z-associated Higgs production. We show results obtained from a merged calculation (solid) and results as obtained from a pure parton-shower simulation (dashed) as well as the ratio of the two (lower panel).

recoiling against the Z boson, despite the latter being massive.

In conclusion, we have seen that loop-induced corrections are of particular relevance at higher collider energies. This was demonstrated by considering their contributions to very inclusive event selections. When applying realistic experimental cuts, these effects can be potentially further enhanced. Furthermore, the description of QCD radiation patterns featuring hard QCD jet emissions can be substantially improved using multijet-merging techniques. Due to the increased partonic energies available at a future hadron collider, such configurations will contribute to the characteristics of typical events to a much larger extent than at the LHC.

V. BACKGROUNDS TO SEARCHES FOR NEW PHYSICS AT 100 TEV

Phenomenological studies at a 100 TeV collider will certainly build on the discoveries and analyses performed at the LHC machine. This section looks at the effects a 100 TeV hadron environment has on typical analyses used to search for beyond the SM (BSM) physics. The search channels investigated are multilepton final states and monojet production.

Multilepton final states constitute a very useful signature for new physics, because they are relatively rare in the SM, and the higher the final-state lepton multiplicity the greater the suppression of SM backgrounds. At the LHC, these final states are used to search for supersymmetric particles, in particular for chargino and neutralino production [114,115]. The dominant SM backgrounds in these searches are multi-V production, for $V = W^{\pm}/Z$, $t\bar{t}$, tZ, $t\bar{t}V$ and $t\bar{t}VV$. The process classes involving top quarks are particularly relevant for analyses which do not contain a b-jet veto. In principle Higgs processes also contribute to the multilepton background, but these shall not be considered here. Instead, the focus of this section is on how weak boson production channels as well as top-quark physics can impact searches at 100 TeV. Current experimental studies at the LHC can be easily extended to a 100 TeV environment, by extending the reach in transverse momenta, missing energy and jet multiplicities.

In contrast to the multilepton analysis, monojet searches veto all events with any leptons or multiple hard jets. The remaining SM processes which can contribute to this final state are then very few, creating a good environment for BSM searches. Any new, weakly interacting (meta)stable particle created will leave the detector as missing energy, which then forms the signal for this type of search. Because of the veto on additional hard QCD radiation, monojet searches are vulnerable at 100 TeV to cutting out large regions of phase space, especially when considering the high-energy regions. The analyses in this paper are based loosely on the monojet studies carried out at the LHC by both the ATLAS [116–119] and CMS [120–122] experiments, which search for hints of dark matter or extra dimensions. The same cuts that are appropriate for the LHC are also applied to the 100 TeV environment, the only alteration being an increase in jet p_T to more suitable values for a 100 TeV collider. This paper therefore investigates the extension of typical LHC monojet searches to the increased phase space available at such high energies, which allows searches for, e.g., the production of particles with masses extending further into the TeV range than is possible at the LHC. The dominant irreducible background in these searches is $Z \to \nu\bar{\nu}$. As well as this, there are significant contributions from processes where leptons have been lost in the analysis. These are $W^{\pm}$, $Z \to \ell^{+}\ell^{-}$ and $t\bar{t}$ production. Two Higgs production channels are also considered in this analysis, gluon fusion and VBF, where in both cases the Higgs is considered to decay to invisibles. The top mass in the gluon fusion production channel is considered by a reweighting of the Born matrix element to include the top loop [100], with OPENLOOPS contributing the virtual matrix element.

A. Setup

The distributions presented in this section are based on matrix-element plus parton-shower simulations and do not include underlying event or hadronization effects. Most processes are considered at LO merged accuracy. The multilepton analysis includes, for the $t\bar{t}$, $W^{\pm}$, Z and diboson processes, the leading matrix element to NLO accuracy with LO matrix elements of higher multiplicities included via the MENLOPS procedure [23]. The renormalization and factorization scales for all processes considered are set using the CKKW prescription [34,47], and the COMIX matrix element generator [31] was used for all LO calculations as well as the real subtraction piece of the NLO calculations. However, for the Born-like contributions to the NLO calculation and the integrated subtraction terms, the AMEGIC++ matrix element generator [123,124] was employed with virtual matrix elements calculated through the interface to OPENLOOPS [17].

For the multilepton final state, single vector-boson production is considered off shell, as are the bosons in $t\bar{t}V$ production. However, in both the monojet analysis and for processes with two or more weak bosons, the narrow-width approximation is used and the decays are factorized from the production. The kinematics of the decay are then redistributed according to a Breit-Wigner distribution, with spin correlations being preserved [125].

B. Analyses

The multilepton analysis is inspired by the ATLAS publication on trilepton searches at the LHC at 8 TeV [114]. The analysis has been extended to include the single-lepton channel as well as the dilepton channel, and all lepton multiplicities are considered exclusive. These analyses are implemented within the RIVET [126] framework.

TABLE IV. The defining cuts for the two phase-space regions considered in the monojet analysis.

Observable	"ΔΦ" selection	"p_T gap" selection
leading jet p_T	0.1 TeV	0.150 TeV
max. p_T subleading jet	N/A	50 GeV
min. missing E_T	0.1 TeV	0.1 TeV
max $\Delta\Phi(j_1, j_2)$	2	N/A

The multilepton analysis shall provide an overview of the behavior of SM multilepton processes at 100 TeV, and the cuts are therefore kept to a minimum. Electrons are dressed with photons within a cone of radius $R = 0.1$ around the electron. Leptons are required to be central, such that $|\eta_\ell| < 2.5$. Jets are defined with the anti-k_T method with FASTJET [30], with $p_T > 20$ GeV and $|y_j| < 5$. Jets which pass the jet definition are further required to be isolated from electrons by at least a distance $\Delta R_{\ell j} > 0.2$. Any jet too close to an electron is rejected. Leptons are then required to be isolated from other leptons. Any two leptons closer than $\Delta R_{\ell\ell} < 0.1$ are both rejected, with the exception of two electrons, when the harder of the pair only is retained. For the Z-veto bin, any event with a pair of same-flavor-opposite-sign (SFOS) leptons is vetoed.

For the monojet analysis, the cuts are based very loosely on corresponding ATLAS and CMS studies at the LHC. One challenge for monojet analyses, which becomes more pronounced in the high-energy regime that will be common at 100 TeV, is the additional QCD radiation that often accompanies hard interactions. In order to study the effect this has on the analyses, two different regions shall be considered. The key difference between the two is that the first analysis, referred to as "p_T gap" selection, places a strict veto on any secondary jet with $p_T > 50$ GeV, but allows a softer second jet while the second analysis, called "ΔΦ" selection, allows one additional jet provided it satisfies cuts that target the dijet background. Both approaches are implemented for this study, along with a variant of the CMS analysis more in line with typical energies for a 100 TeV collider. Any event with leptonic activity is vetoed for this analysis. Jets are defined with the anti-k_T method with a radius parameter $R = 0.4$, $p_T > 20$ GeV and $|y_j| < 5$. The cuts defining the different regions are summarized in Table IV.

C. Multilepton analyses

The H_T distribution, i.e. the scalar sum of the transverse momenta of all final-state objects in the event, including the missing E_T, is shown in Fig. 23, binned in terms of the exclusive lepton multiplicity. This observable provides an overview of the relative contributions of the different processes, with $t\bar{t}$ dominating the one- and two-lepton cases and $W^\pm Z$ dominating the three-lepton final state. Comparing the two plots in the middle and lower lines of Fig. 23 shows the effect of introducing the Z-boson veto. This addition clearly suppresses the Z-boson production processes in both the two-lepton and the three-lepton channels, and thus significantly reduces the overall size of the SM background in this search channel. However, in the missing E_T distribution shown in Fig. 24, this veto does not have such a dramatic effect in the two-lepton channel as in the three-lepton channel. Comparing the left-hand and right-hand plots of the middle (two-lepton) line as before, Fig. 24 shows a significant suppression of the background in the low-missing-E_T region, but in the high-energy tail of the distribution, $t\bar{t}$ production is dominant in the dilepton bin even before the Z-boson veto is applied, and as such there is only a small impact on the high-energy tail of the background processes for the missing E_T distribution due to the Z-boson veto. Because the $t\bar{t}$ process does not contribute to the three-lepton channel, the Z-boson veto has a similar effect on the missing E_T distribution as it had on the H_T distribution. Despite the Z-boson veto, $W^\pm Z$ production continues to be the dominant background, with $t\bar{t}W^\pm$ contributing significantly in the higher-H_T or missing-E_T tails of the distribution. It is therefore important in trilepton final-state searches with a Z-boson veto to have good control of the $t\bar{t}W^\pm$ process, at least to NLO precision [15,127–129].

Figure 23 demonstrates the very large reach in scales the 100 TeV FCC provides. The tails of the H_T distributions easily stretch out to 10 TeV. However, it can also be seen that the H_T distribution becomes increasingly soft the higher the lepton multiplicity. Nevertheless, Fig. 23 impressively demonstrates the importance to have control of these background SM processes in the multi-TeV regime and that indeed many processes need to be taken into account.

Figure 24 shows the missing energy distribution for the considered set of processes. This observable is particularly relevant for BSM searches, where the signal expected is an excess at large missing energy. At a 100 TeV proton-proton collider, Fig. 24 shows that a significant amount of SM background is present at these large missing-E_T values. For the three-lepton final state the dominant background is given by $W^\pm Z$ production. For the two-lepton bin with a Z veto implemented, $t\bar{t}$ is the dominant process for most of the distribution. However, at high E_T^{miss}, W^+W^- is also significant. It is therefore crucial to have a very good description of both $t\bar{t}$ and W^+W^- in these phase-space regions in order to claim sensitivity for new physics at this scale. In fact, for both channels the complete set of NNLO QCD corrections is known [130,131]. For the low-E_T^{miss} regime at around 50 GeV for the two-lepton bin with no Z-boson veto, both Z production and $t\bar{t}$ production are significant, although $t\bar{t}$ still dominates in the tail of the distribution. For the one-lepton bin, for a large amount of the distribution both $W^\pm$ and $t\bar{t}$ production are significant.

The suppression of the SM backgrounds with increasing lepton multiplicity can be clearly seen in Figs. 23 and 24.

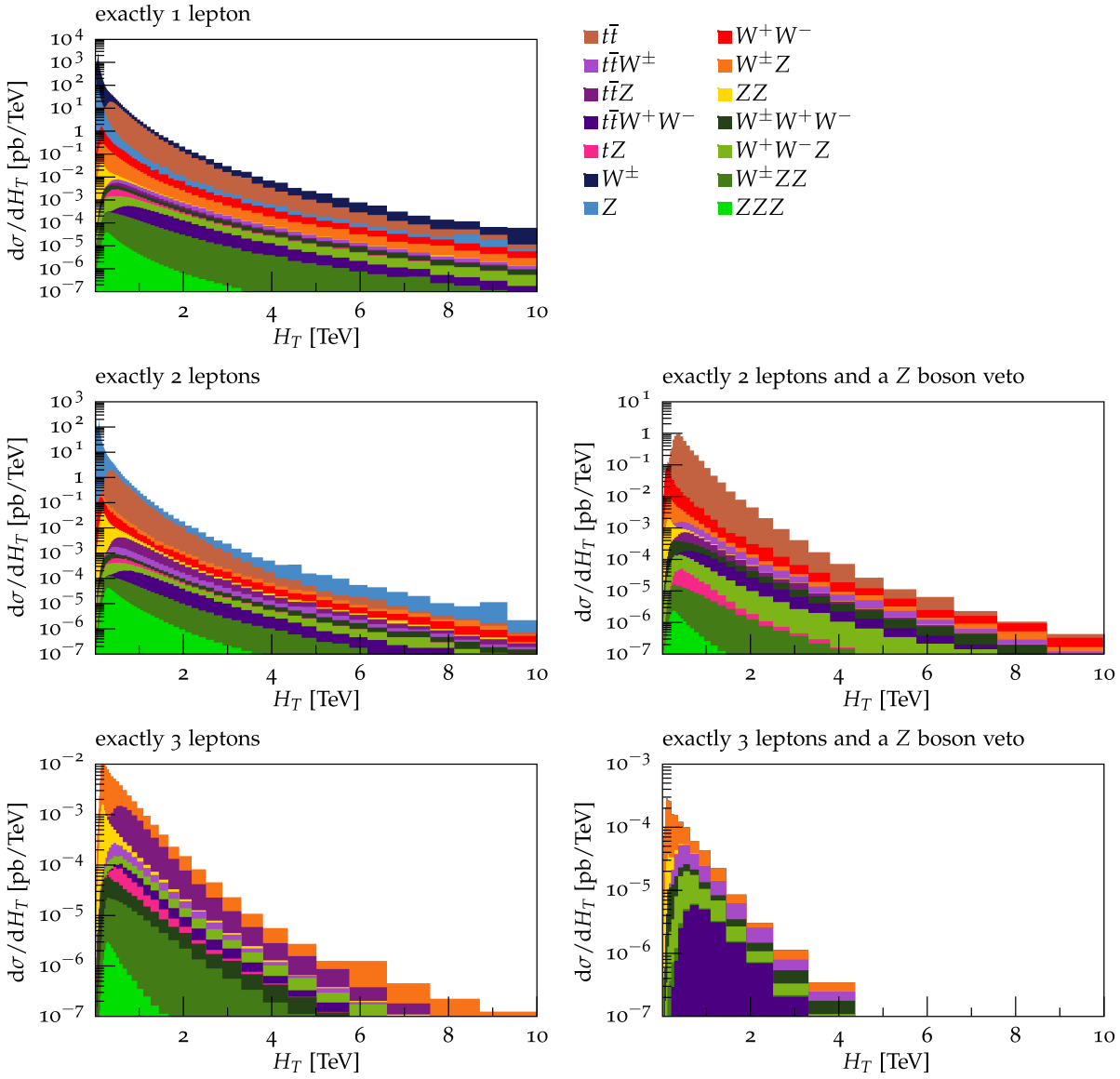

FIG. 23. The H_T distributions for various SM backgrounds in multilepton searches, depicted for different lepton multiplicities. The right-hand plots in the lower two rows show the effect of including a veto on SFOS lepton pairs. The distributions are merged with up to three additional light QCD partons for V and VV production, and up to two additional light partons for all other processes with a merging scale of $Q_{\text{cut}} = 30$ GeV.

However, even for the trilepton final state the SM processes can reach $\mathcal{O}(1\text{ TeV})$ in E_T^{miss} and the H_T distribution can reach very high values, up to $\mathcal{O}(10\text{ TeV})$.

D. Monojet searches

The current approaches to monojet studies, as outlined in the Introduction, allow for additional QCD radiation, although to different extents. This is necessary in order to increase the overall signal yield, and becomes increasingly important the higher the collider energy. Therefore, in order for monojet searches to take advantage of the increased energy of collisions at a 100 TeV collider, they must be sufficiently inclusive to this additional QCD radiation. Figures 25 and 26 show the number of jets in each event which pass all cuts but trigger the veto on QCD activity. Accordingly, the zero-jet bin contains the total cross section of events passing the analysis cuts. The results are given for different values of the minimum leading jet p_T, and show how the average number of jets in the events increases with increasing jet p_T. Figure 25 shows the results for the "$\Delta\Phi$" region, where a subleading jet above $p_T = 30$ GeV with $\Delta\Phi_{j_1 j_2} < 2$ is allowed. Figure 26 shows the results for the "p_T gap" region, which requires any subleading jet to have $p_T < 50$ GeV. Both approaches show that at low values of leading jet p_T, there is a good proportion of events that pass the cuts on QCD radiation.

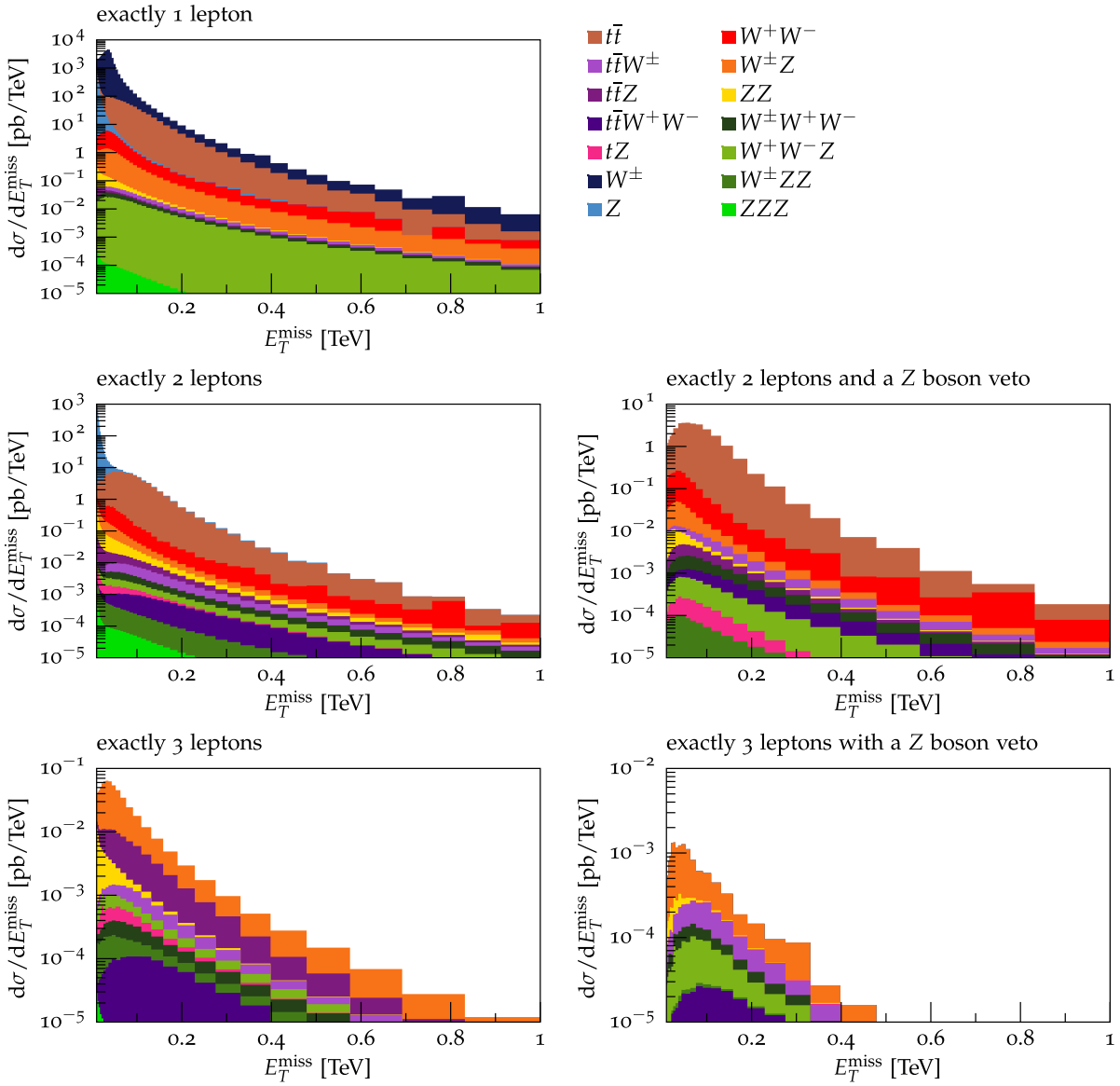

FIG. 24. E_T^{miss} distributions for various SM backgrounds in multilepton searches, depicted for different lepton multiplicities. The right-hand plots in the lower two rows show the effect of including a veto on SFOS lepton pairs. Calculational details are as quoted in Fig. 23.

However, as the leading jet becomes harder, an increasing number of events are vetoed. In all of the plots, the $t\bar{t}$ background is the most suppressed by the QCD radiation veto in the high-p_T region, while the irreducible background of $Z \to \nu\bar{\nu}$ is the most dominant contribution that passes the cuts, as well as in the bins of lower jet multiplicity.

For leading jet $p_T > 0.1$ TeV, the average number of veto jets in the "$\Delta\Phi$" selection, cf. Fig. 25, is 1.2, compared to 1.5 for the "p_T gap" selection, cf. Fig. 26. The corresponding jet-veto probabilities are 52% ("$\Delta\Phi$" selection) compared to 67% ("p_T gap" selection). However, for $p_{Tj_1} > 0.5$ TeV and above, the two different approaches give very similar distributions. In the highest p_T region considered here, $p_{Tj_1} > 2$ TeV, there is an average number of vetoed jets of 3.8(1) [3.7(1)] resulting in a jet-veto probability of 99.7% (99.8%) for the "$\Delta\Phi$" ("p_T gap") analysis. Neither approach appears to be better suited to dealing with the typical high energies of a 100 TeV collider. This implies that monojet searches as they have been implemented at the LHC would not be very sensitive to searches in the high-p_T phase-space regions; a more considered treatment of high levels of QCD activity is necessary for a monojet search at 100 TeV.

Figures 27 and 28 show the E_T^{miss} and leading jet p_T distributions, respectively, for both the "$\Delta\Phi$" and the "p_T gap" selections. Figure 27 shows very similar behavior of the E_T^{miss} distribution between the two regimes, beyond the low-p_T effects from the higher leading jet p_T cut in the "p_T gap" analysis. Here the $Z \to \nu\bar{\nu}$ process is dominant

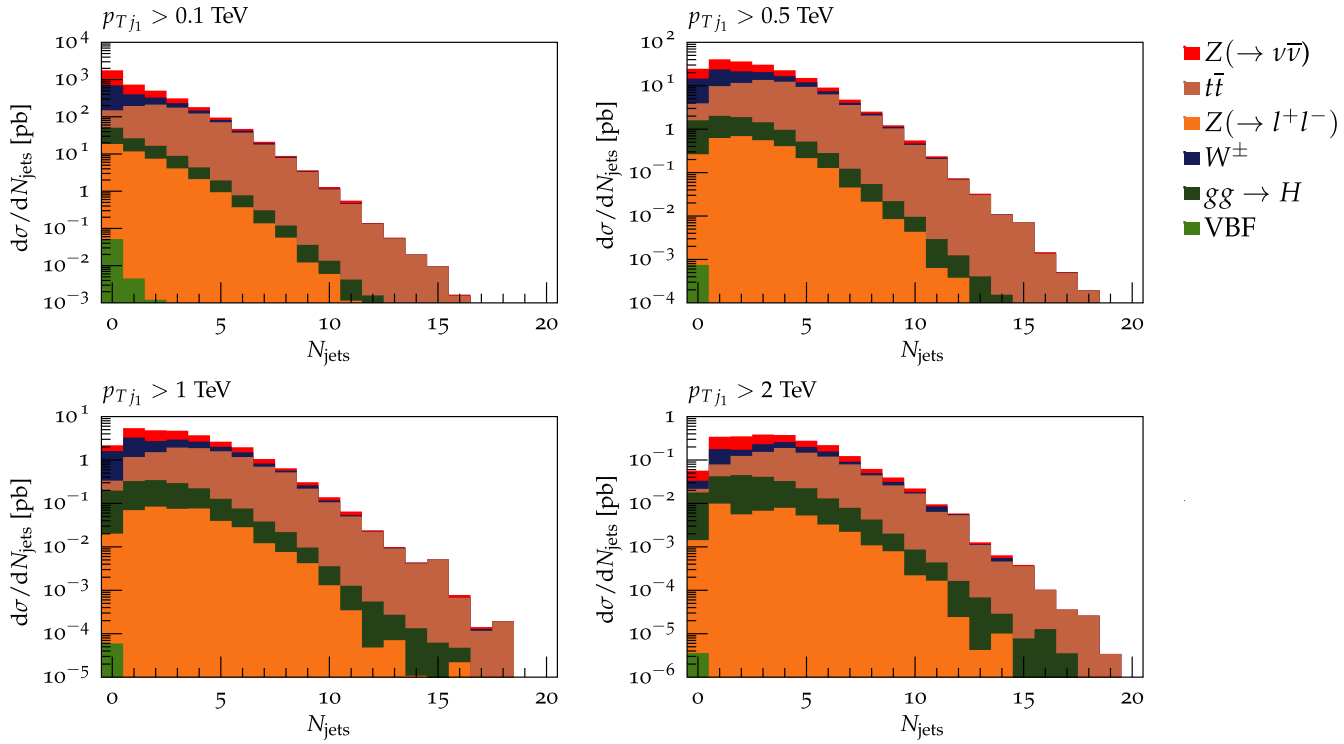

FIG. 25. Number of jet candidates vetoed for the "ΔΦ" selection binned by leading jet transverse momentum. The top-left (top-right) plot shows the result for $p_{Tj_1} > 0.1$ TeV ($p_{Tj_1} > 0.5$ TeV), while the bottom-left (bottom-right) shows the result for the high-p_T region, i.e. $p_{Tj_1} > 1$ TeV ($p_{Tj_1} > 2$ TeV).

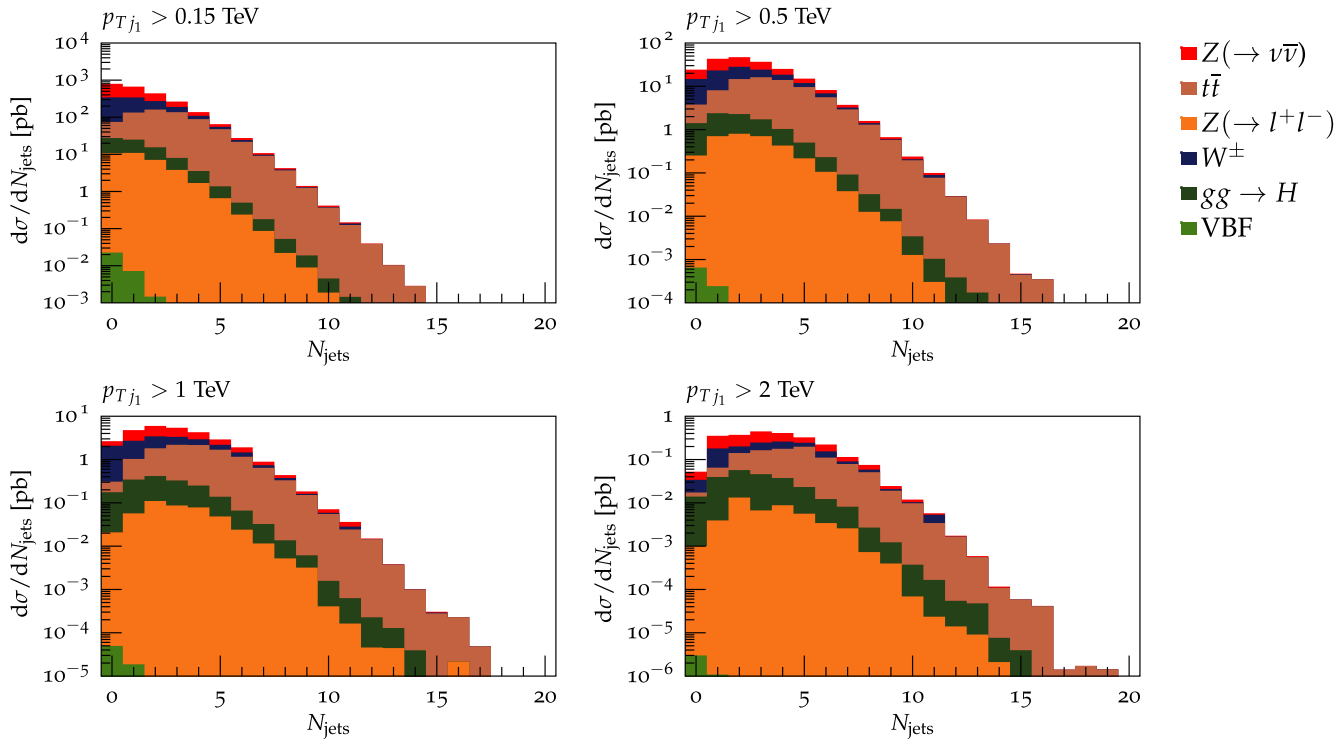

FIG. 26. Number of jet candidates vetoed for the "p_T gap" selection binned by leading jet p_T. The top-left plot shows the result for $p_{Tj_1} > 0.15$ TeV, the top-right for $p_{Tj_1} > 0.5$ TeV and the bottom-left (bottom-right) for $p_{Tj_1} > 1$ TeV ($p_{Tj_1} > 2$ TeV).

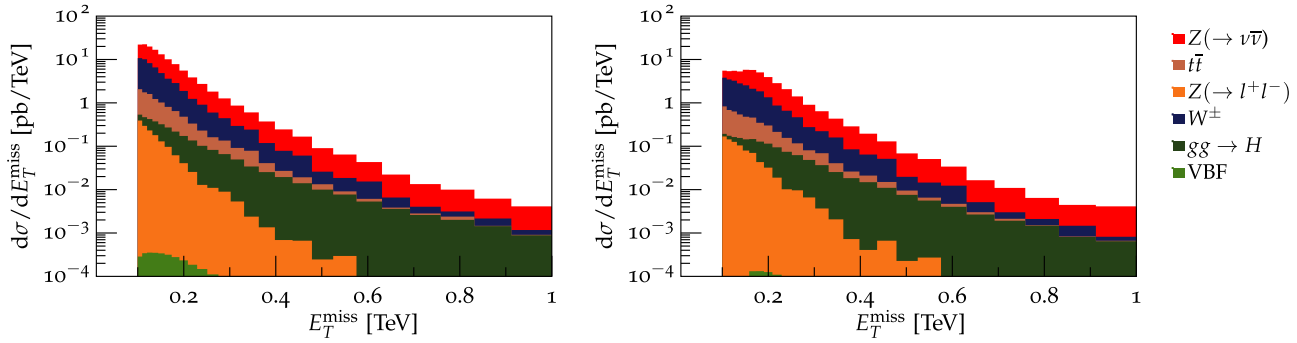

FIG. 27. The missing energy distribution for the "$\Delta\Phi$" selection (left panel), and for the "p_T gap" selection (right panel).

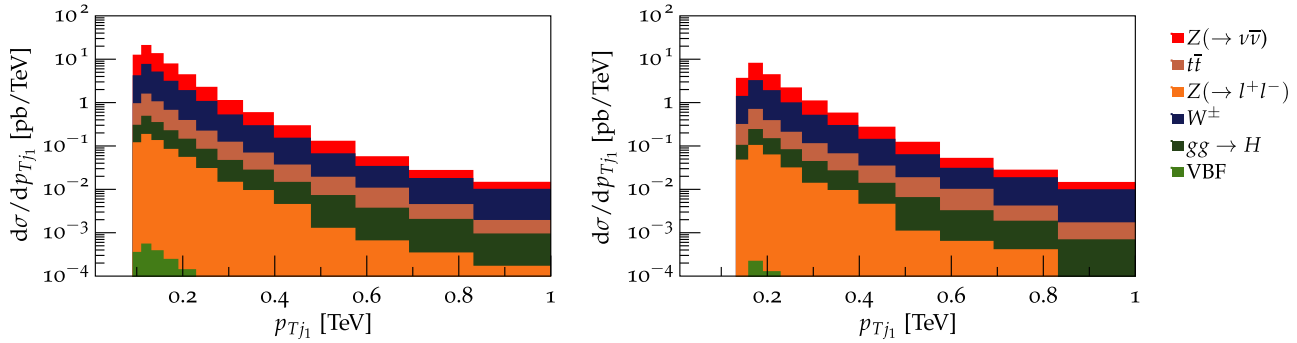

FIG. 28. The leading jet p_T distribution for the "$\Delta\Phi$" selection (left panel), and for the "p_T gap" selection (right panel).

throughout the distribution, with $W^\pm$ production being the leading subdominant background. The $t\bar{t}$ process is most significant in the lower E_T^{miss} bins, and does not contribute significantly in the tail of the distribution. Instead, the $gg \to H$ process becomes the most dominant subleading background at large E_T^{miss}.

The hierarchy of processes is similar in Fig. 28 when comparing to Fig. 27. The $Z \to \nu\bar{\nu}$ process is dominant throughout the distribution, and $W^\pm$ production is the leading subdominant contribution. In contrast to the E_T^{miss} distribution, however, the relative contributions of the SM processes to the leading jet p_T distribution remain more constant in the high-energy tail. The $t\bar{t}$ process does not disappear in the high-p_T tail of the distribution as happens in Fig. 27, and similarly the $gg \to H$ production does not become the subleading background at large leading jet p_T. Figures 27 and 28, show the "$\Delta\Phi$" and "p_T gap" approaches leading to distributions with similar reaches in the E_T^{miss} and p_{Tj_1} distributions. Even with the large suppression from the veto on multiple QCD radiation, the monojet analysis could probe energies up to 1 TeV at a 100 TeV hadron collider, a reach which could be extended with a dedicated study into the relevant phase-space cuts for such a high-energy environment. A 100 TeV collider therefore provides an excellent searching ground for new physics, which could be explored with monojet analyses which build on those performed at the LHC.

VI. CONCLUSIONS

This paper presented results demonstrating the range of substantial theoretical challenges a future 100 TeV hadron collider would create.

In the first half of this paper we employed techniques capturing dominant scaling patterns to extrapolate known fixed-order results for multijet production in different kinematic regimes to higher multiplicities or different regimes. In so doing we identified regimes typical for the emergence of Poisson scaling and staircase scaling, with good agreement between scaling-based predictions and simulation results in both cases. We also addressed jet-substructure techniques at 100 TeV. This is interesting from the point of view of quark-gluon discrimination, as well as identifying the fat jets of highly boosted particles, such as top quarks and $W^\pm$-bosons. Because the center-of-mass energy is so large, the possibility of having a highly boosted heavy particle is much larger than at LHC energies. The number of subjets was found to provide a sensible probe to the initiating particle's color charge. It was also established that the parton shower is in good agreement with analytical results, to NDLA accuracy.

At high energies, the proton begins to be probed at smaller and smaller values of Bjorken x. The gluon PDF becomes more dominant in this region, and it was shown in this paper that the loop-induced processes for vector-boson production and Higgs-boson production become more

significant in this regime. As is well known, HEFT is not a reliable approximation in the high-p_T tail or high-mass regime of Higgs-boson production through gluon fusion due to top-mass effects. Their effect becomes more relevant at a 100 TeV machine, due to the increased phase space it provides. The final section in this paper looked at the effects the 100 TeV environment would have on some typical LHC analyses for BSM searches. It was seen that the reach of these searches can extend much further in p_T, and that while the multilepton analyses are already well suited for 100 TeV searches, jet vetoes at relatively low values in monojet searches can cut out a lot of interesting phase space, particularly in the high-p_T regions due to the typically large amount of QCD radiation of the 100 TeV environment.

A 100 TeV collider will provide several new challenges. It will have an overwhelming amount of QCD radiation, and this paper has shown that although some techniques used at the LHC can be used to study a 100 TeV environment, others will need to be adapted or improved. Loop-induced production channels will become far more significant, and will deserve theoretical work to improve our understanding to match the control requirements necessary. Moving to such a high energy comes with a large amount of increased complexity and challenges, but also a very large potential for the discovery of new physics and tests of the current SM.

ACKNOWLEDGMENTS

The authors are grateful to their coworkers in the SHERPA Collaboration. We acknowledge financial support by the European Commission through the networks MCnetITN (PITN–GA–2012–315877) and HiggsTools (PITN–GA–2012–316704). E. B. and S. S. acknowledge financial support from BMBF under Contract No. 05H15MGCAA.

[1] G. Aad *et al.* (ATLAS Collaboration), Observation of a new particle in the search for the Standard Model Higgs boson with the ATLAS detector at the LHC, Phys. Lett. B **716**, 1 (2012).
[2] S. Chatrchyan *et al.* (CMS Collaboration), Observation of a new boson at a mass of 125 GeV with the CMS experiment at the LHC, Phys. Lett. B **716**, 30 (2012).
[3] F. Englert and R. Brout, Broken Symmetry and the Mass of Gauge Vector Mesons, Phys. Rev. Lett. **13**, 321 (1964).
[4] P. W. Higgs, Broken symmetries, massless particles and gauge fields, Phys. Lett. **12**, 132 (1964).
[5] P. W. Higgs, Broken Symmetries and the Masses of Gauge Bosons, Phys. Rev. Lett. **13**, 508 (1964).
[6] G. S. Guralnik, C. R. Hagen, and T. W. B. Kibble, Global Conservation Laws and Massless Particles, Phys. Rev. Lett. **13**, 585 (1964).
[7] N. Arkani-Hamed, T. Han, M. Mangano, and L.-T. Wang, Physics opportunities of a 100 TeV proton-proton collider, arXiv:1511.06495.
[8] A. Avetisyan *et al.*, Methods and results for Standard Model event generation at $\sqrt{s} = 14$ TeV, 33 TeV and 100 TeV proton colliders, in Community Summer Study 2013: Snowmass on the Mississippi (CSS2013), Minneapolis, MN, 2013 (to be published).
[9] I. Hinchliffe, A. Kotwal, M. L. Mangano, C. Quigg, and L.-T. Wang, Luminosity goals for a 100-TeV pp collider, Int. J. Mod. Phys. A **30**, 1544002 (2015).
[10] D. d'Enterria and T. Pierog, Global properties of proton-proton collisions at $\sqrt{s} = 100$ TeV, arXiv:1604.08536.
[11] A. Buckley *et al.*, General-purpose event generators for LHC physics, Phys. Rep. **504**, 145 (2011).
[12] T. Carli, K. Rabbertz, and S. Schumann, Studies of quantum chromodynamics at the LHC, in *The Large Hadron Collider: Harvest of Run 1*, edited by T. Schörner-Sadenius (Springer, New York, 2015), p. 139.
[13] G. Ossola, C. G. Papadopoulos, and R. Pittau, CutTools: A program implementing the OPP reduction method to compute one-loop amplitudes, J. High Energy Phys. 03 (2008) 042.
[14] A. van Hameren, C. Papadopoulos, and R. Pittau, Automated one-loop calculations: A proof of concept, J. High Energy Phys. 09 (2009) 106.
[15] V. Hirschi, R. Frederix, S. Frixione, M. V. Garzelli, F. Maltoni, and R. Pittau, Automation of one-loop QCD corrections, J. High Energy Phys. 05 (2011) 044.
[16] G. Cullen, N. Greiner, G. Heinrich, G. Luisoni, P. Mastrolia, G. Ossola, T. Reiter, and F. Tramontano, Automated one-loop calculations with GoSam, Eur. Phys. J. C **72**, 1889 (2012).
[17] F. Cascioli, P. Maierhöfer, and S. Pozzorini, Scattering Amplitudes with Open Loops, Phys. Rev. Lett. **108**, 111601 (2012).
[18] A. Denner, S. Dittmaier, and L. Hofer, Collier: A fortran-based complex one-loop library in extended regularizations, arXiv:1604.06792.
[19] S. Catani, F. Krauss, R. Kuhn, and B. R. Webber, QCD matrix elements + parton showers, J. High Energy Phys. 11 (2001) 063.
[20] S. Frixione and B. R. Webber, Matching NLO QCD computations and parton shower simulations, J. High Energy Phys. 06 (2002) 029.
[21] P. Nason, A new method for combining NLO QCD with shower Monte Carlo algorithms, J. High Energy Phys. 11 (2004) 040.
[22] S. Höche, F. Krauss, M. Schönherr, and F. Siegert, Next-to-leading order matrix elements and truncated showers, arXiv:1009.1477.

[23] S. Höche, F. Krauss, M. Schönherr, and F. Siegert, NLO matrix elements and truncated showers, J. High Energy Phys. 08 (2011) 123.

[24] L. Lönnblad and S. Prestel, Merging multi-leg NLO matrix elements with parton showers, J. High Energy Phys. 03 (2013) 166.

[25] T. Sjöstrand, S. Ask, J. R. Christiansen, R. Corke, N. Desai, P. Ilten, S. Mrenna, S. Prestel, C. O. Rasmussen, and P. Z. Skands, An introduction to PYTHIA 8.2, Comput. Phys. Commun. **191**, 159 (2015).

[26] J. Bellm *et al.*, HERWIG7.0/HERWIG++ 3.0 release note, Eur. Phys. J. C **76**, 196 (2016).

[27] T. Gleisberg, S. Höche, F. Krauss, A. Schälicke, S. Schumann, and J. Winter, SHERPA1.α, a proof-of-concept version, J. High Energy Phys. 02 (2004) 056.

[28] T. Gleisberg, S. Höche, F. Krauss, M. Schönherr, S. Schumann, F. Siegert, and J. Winter, Event generation with SHERPA1.1, J. High Energy Phys. 02 (2009) 007.

[29] M. Cacciari, G. P. Salam, and G. Soyez, The anti-$k(t)$ jet clustering algorithm, J. High Energy Phys. 04 (2008) 063.

[30] M. Cacciari, G. P. Salam, and G. Soyez, FastJet user manual, Eur. Phys. J. C **72**, 1896 (2012).

[31] T. Gleisberg and S. Höche, COMIX, a new matrix element generator, J. High Energy Phys. 12 (2008) 039.

[32] R. D. Ball *et al.* (NNPDF Collaboration), Parton distributions for the LHC Run II, J. High Energy Phys. 04 (2015) 040.

[33] F. Krauss, Matrix elements and parton showers in hadronic interactions, J. High Energy Phys. 08 (2002) 015.

[34] S. Höche, F. Krauss, S. Schumann, and F. Siegert, QCD matrix elements and truncated showers, J. High Energy Phys. 05 (2009) 053.

[35] L. Lönnblad, Correcting the colour-dipole cascade model with fixed order matrix elements, J. High Energy Phys. 05 (2002) 046.

[36] L. Lönnblad and S. Prestel, Matching tree-level matrix elements with interleaved showers, J. High Energy Phys. 03 (2012) 019.

[37] L. Lönnblad and S. Prestel, Unitarising matrix element + parton shower merging, J. High Energy Phys. 02 (2013) 094.

[38] M. L. Mangano, M. Moretti, and R. Pittau, Multijet matrix elements and shower evolution in hadronic collisions: $Wb\bar{b} + n$-jets as a case study, Nucl. Phys. **B632**, 343 (2002).

[39] M. L. Mangano, M. Moretti, F. Piccinini, and M. Treccani, Matching matrix elements and shower evolution for top-pair production in hadronic collisions, J. High Energy Phys. 01 (2007) 013.

[40] K. Hamilton, P. Richardson, and J. Tully, A modified CKKW matrix element merging approach to angular-ordered parton showers, J. High Energy Phys. 11 (2009) 038.

[41] J. Alwall *et al.*, Comparative study of various algorithms for the merging of parton showers and matrix elements in hadronic collisions, Eur. Phys. J. C **53**, 473 (2008).

[42] Z. Nagy and D. E. Soper, Matching parton showers to NLO computations, J. High Energy Phys. 10 (2005) 024.

[43] S. Schumann and F. Krauss, A parton shower algorithm based on Catani-Seymour dipole factorization, J. High Energy Phys. 03 (2008) 038.

[44] S. Höche, F. Krauss, M. Schönherr, and F. Siegert, A critical appraisal of NLO + PS matching methods, J. High Energy Phys. 09 (2012) 049.

[45] S. Höche, F. Krauss, M. Schönherr, and F. Siegert, $W + n$-jet Predictions with MC@NLO in SHERPA, Phys. Rev. Lett. **110**, 052001 (2013).

[46] T. Gehrmann, S. Höche, F. Krauss, M. Schönherr, and F. Siegert, NLO QCD matrix elements + parton showers in $e^+e^- \to$ hadrons, J. High Energy Phys. 01 (2013) 144.

[47] S. Höche, F. Krauss, M. Schönherr, and F. Siegert, QCD matrix elements + parton showers: The NLO case, J. High Energy Phys. 04 (2013) 027.

[48] S. Frixione, P. Nason, and G. Ridolfi, A positive-weight next-to-leading-order Monte Carlo for heavy flavor hadroproduction, J. High Energy Phys. 09 (2007) 126.

[49] R. Frederix and S. Frixione, Merging meets matching in MC@NLO, J. High Energy Phys. 12 (2012) 061.

[50] J.-C. Winter, F. Krauss, and G. Soff, A modified cluster-hadronization model, Eur. Phys. J. C **36**, 381 (2004).

[51] S. Alekhin *et al.*, HERA and the LHC—A workshop on the implications of HERA for LHC physics: Proceedings—Part A, arXiv:hep-ph/0601012.

[52] M. Schönherr and F. Krauss, Soft photon radiation in particle decays in SHERPA, J. High Energy Phys. 12 (2008) 018.

[53] A. Denner, S. Dittmaier, M. Roth, and D. Wackeroth, $O(\alpha)$ corrections to $e^+e^- \to W^+W^- \to$ four fermions(+ gamma): First numerical results from RACOON W W, Phys. Lett. B **475**, 127 (2000).

[54] C. F. Berger, Z. Bern, L. J. Dixon, F. Febres-Cordero, D. Forde, H. Ita, D. A. Kosower, and D. Maître, Automated implementation of on-shell methods for one-loop amplitudes, Phys. Rev. D **78**, 036003 (2008).

[55] E. Gerwick, S. Schumann, B. Gripaios, and B. Webber, QCD jet rates with the inclusive generalized k_t algorithms, J. High Energy Phys. 04 (2013) 089.

[56] E. Gerwick, Recursive prescription for logarithmic jet rate coefficients, Phys. Rev. D **88**, 094009 (2013).

[57] M. Dasgupta, F. Dreyer, G. P. Salam, and G. Soyez, Small-radius jets to all orders in QCD, J. High Energy Phys. 04 (2015) 039.

[58] E. Gerwick, T. Plehn, S. Schumann, and P. Schichtel, Scaling patterns for QCD jets, J. High Energy Phys. 10 (2012) 162.

[59] G. Aad *et al.* (ATLAS Collaboration), Measurement of multi-jet cross sections in proton-proton collisions at a 7 TeV center-of-mass energy, Eur. Phys. J. C **71**, 1763 (2011).

[60] G. Aad *et al.* (ATLAS Collaboration), Measurement of the production cross section of jets in association with a Z boson in pp collisions at $\sqrt{s} = 7$ TeV with the ATLAS detector, J. High Energy Phys. 07 (2013) 032.

[61] G. Aad *et al.* (ATLAS Collaboration), Measurements of the W production cross sections in association with jets with the ATLAS detector, Eur. Phys. J. C **75**, 82 (2015).

[62] V. Khachatryan *et al.* (CMS Collaboration), Differential cross section measurements for the production of a W

boson in association with jets in proton-proton collisions at $\sqrt{s} = 7$ TeV, Phys. Lett. B **741**, 12 (2015).
[63] C. Englert, T. Plehn, P. Schichtel, and S. Schumann, Jets plus missing energy with an autofocus, Phys. Rev. D **83**, 095009 (2011).
[64] C. Englert, T. Plehn, P. Schichtel, and S. Schumann, Establishing jet scaling patterns with a photon, J. High Energy Phys. 02 (2012) 030.
[65] Z. Bern, L. Dixon, F. Febres Cordero, S. Höche, H. Ita, D. Kosower, and D. Maítre, Extrapolating W-associated jet-production ratios at the LHC, Phys. Rev. D **92**, 014008 (2015).
[66] E. Gerwick and P. Schichtel, Jet properties at high-multiplicity, arXiv:1412.1806.
[67] M. E. Peskin and D. V. Schroeder, *An Introduction to Quantum Field Theory* (Westview, Boulder, CO, 1995).
[68] S. El Hedri, A. Hook, M. Jankowiak, and J. G. Wacker, Learning how to count: A high multiplicity search for the LHC, J. High Energy Phys. 08 (2013) 136.
[69] M. Rubin, G. P. Salam, and S. Sapeta, Giant QCD K-factors beyond NLO, J. High Energy Phys. 09 (2010) 084.
[70] S. Chatrchyan *et al.* (CMS Collaboration), Event shapes and azimuthal correlations in $Z +$ jets events in pp collisions at $\sqrt{(s)} = 7$ TeV, Phys. Lett. B **722**, 238 (2013).
[71] CMS Collaboration, Particle-flow event reconstruction in CMS and performance for jets, taus, and MET, Report No. CMS-PAS-PFT-09-001.
[72] M. A. Thomson, Particle flow calorimetry and the PandoraPFA algorithm, Nucl. Instrum. Methods Phys. Res., Sect. A **611**, 25 (2009).
[73] S. Schätzel and M. Spannowsky, Tagging highly boosted top quarks, Phys. Rev. D **89**, 014007 (2014).
[74] A. J. Larkoski and J. Thaler, Aspects of jets at 100 TeV, Phys. Rev. D **90**, 034010 (2014).
[75] T. Cohen, R. T. D'Agnolo, M. Hance, H. K. Lou, and J. G. Wacker, Boosting stop searches with a 100 TeV proton collider, J. High Energy Phys. 11 (2014) 021.
[76] A. J. Larkoski, F. Maltoni, and M. Selvaggi, Tracking down hyper-boosted top quarks, J. High Energy Phys. 06 (2015) 032.
[77] A. Abdesselam *et al.*, Boosted objects: A probe of beyond the standard model physics, Eur. Phys. J. C **71**, 1661 (2011).
[78] T. Plehn and M. Spannowsky, Top tagging, J. Phys. G **39**, 083001 (2012).
[79] A. Altheimer *et al.*, Jet substructure at the Tevatron and LHC: New results, new tools, new benchmarks, J. Phys. G **39**, 063001 (2012).
[80] A. Altheimer *et al.*, Boosted objects and jet substructure at the LHC. Report of BOOST2012, held at IFIC Valencia, 23rd–27th of July 2012, Eur. Phys. J. C **74**, 2792 (2014).
[81] M. Dasgupta, A. Fregoso, S. Marzani, and G. P. Salam, Towards an understanding of jet substructure, J. High Energy Phys. 09 (2013) 029.
[82] M. Dasgupta, A. Fregoso, S. Marzani, and A. Powling, Jet substructure with analytical methods, Eur. Phys. J. C **73**, 2623 (2013).
[83] A. J. Larkoski, S. Marzani, G. Soyez, and J. Thaler, Soft drop, J. High Energy Phys. 05 (2014) 146.
[84] M. Dasgupta, L. Schunk, and G. Soyez, Jet shapes for boosted jet two-prong decays from first-principles, J. High Energy Phys. 04 (2016) 166.
[85] A. J. Larkoski, I. Moult, and D. Neill, Analytic boosted boson discrimination, J. High Energy Phys. 05 (2016) 117.
[86] C. Frye, A. J. Larkoski, M. D. Schwartz, and K. Yan, Factorization for groomed jet substructure beyond the next-to-leading logarithm, J. High Energy Phys. 07 (2016) 064.
[87] J. Gallicchio and M. D. Schwartz, Quark and Gluon Tagging at the LHC, Phys. Rev. Lett. **107**, 172001 (2011).
[88] B. Bhattacherjee, S. Mukhopadhyay, M. M. Nojiri, Y. Sakaki, and B. R. Webber, Associated jet and subjet rates in light-quark and gluon jet discrimination, J. High Energy Phys. 04 (2015) 131.
[89] S. Höche and S. Prestel, The midpoint between dipole and parton showers, Eur. Phys. J. C **75**, 461 (2015).
[90] S. Catani, Y. L. Dokshitzer, M. H. Seymour, and B. R. Webber, Longitudinally-invariant $k_\perp$-clustering algorithms for hadron–hadron collisions, Nucl. Phys. **B406**, 187 (1993).
[91] Y. L. Dokshitzer, G. D. Leder, S. Moretti, and B. R. Webber, Better jet clustering algorithms, J. High Energy Phys. 08 (1997) 001.
[92] M. Dasgupta, F. A. Dreyer, G. P. Salam, and G. Soyez, Inclusive jet spectrum for small-radius jets, J. High Energy Phys. 06 (2016) 057.
[93] Y. Delenda, R. Appleby, M. Dasgupta, and A. Banfi, On QCD resummation with $k(t)$ clustering, J. High Energy Phys. 12 (2006) 044.
[94] S. Marzani, R. D. Ball, V. Del Duca, S. Forte, and A. Vicini, Higgs production via gluon-gluon fusion with finite top mass beyond next-to-leading order, Nucl. Phys. **B800**, 127 (2008).
[95] A. Pak, M. Rogal, and M. Steinhauser, Virtual three-loop corrections to Higgs boson production in gluon fusion for finite top quark mass, Phys. Lett. B **679**, 473 (2009).
[96] A. Pak, M. Rogal, and M. Steinhauser, Finite top quark mass effects in NNLO Higgs boson production at LHC, J. High Energy Phys. 02 (2010) 025.
[97] R. V. Harlander, H. Mantler, S. Marzani, and K. J. Ozeren, Higgs production in gluon fusion at next-to-next-to-leading order QCD for finite top mass, Eur. Phys. J. C **66**, 359 (2010).
[98] R. V. Harlander and K. J. Ozeren, Finite top mass effects for hadronic Higgs production at next-to-next-to-leading order, J. High Energy Phys. 11 (2009) 088.
[99] R. V. Harlander and K. J. Ozeren, Top mass effects in Higgs production at next-to-next-to-leading order QCD: Virtual corrections, Phys. Lett. B **679**, 467 (2009).
[100] M. Buschmann, D. Goncalves, S. Kuttimalai, M. Schonherr, F. Krauss, and T. Plehn, Mass effects in the Higgs-gluon coupling: Boosted vs off-shell production, J. High Energy Phys. 02 (2015) 038.
[101] R. Frederix, S. Frixione, E. Vryonidou, and M. Wiesemann, Heavy-quark mass effects in Higgs plus jets production, arXiv:1604.03017.
[102] U. Baur and E. Glover, Higgs boson production at large transverse momentum in hadronic collisions, Nucl. Phys. **B339**, 38 (1990).

[103] R. Ellis, I. Hinchliffe, M. Soldate, and J. V. D. Bij, Higgs decay to $\tau\tau$—A possible signature of intermediate mass Higgs bosons at high energy hadron colliders, Nucl. Phys. **B297**, 221 (1988).

[104] The OpenLoops one-loop generator by F. Cascioli, J. Lindert, P. Maierhöfer and S. Pozzorini is publicly available at http://openloops.hepforge.org.

[105] A. Denner, S. Dittmaier, and L. Hofer, COLLIER—A fortran-library for one-loop integrals, *Proc. Sci.*, LL2014 (2014) 071.

[106] R. V. Harlander, T. Neumann, K. J. Ozeren, and M. Wiesemann, Top-mass effects in differential Higgs production through gluon fusion at order α_s^4, J. High Energy Phys. 08 (2012) 139.

[107] M. Buschmann, C. Englert, D. Goncalves, T. Plehn, and M. Spannowsky, Resolving the Higgs-gluon coupling with jets, Phys. Rev. D **90**, 013010 (2014).

[108] N. Greiner, S. Höche, G. Luisoni, M. Schönherr, J.-C. Winter, and V. Yundin, Phenomenological analysis of Higgs boson production through gluon fusion in association with jets, J. High Energy Phys. 01 (2016) 169.

[109] U. Baur, T. Plehn, and D. L. Rainwater, Measuring the Higgs Boson Self Coupling at the LHC and Finite Top Mass Matrix Elements, Phys. Rev. Lett. **89**, 151801 (2002).

[110] T. Binoth, M. Ciccolini, N. Kauer, and M. Kramer, Gluon-induced W-boson pair production at the LHC, J. High Energy Phys. 12 (2006) 046.

[111] C. Zecher, T. Matsuura, and J. J. van der Bij, Leptonic signals from off-shell Z boson pairs at hadron colliders, Z. Phys. C **64**, 219 (1994).

[112] D. Goncalves, F. Krauss, S. Kuttimalai, and P. Maierhfer, Higgs-strahlung: Merging the NLO Drell-Yan and loop-induced $0+1$ jet multiplicities, Phys. Rev. D **92**, 073006 (2015).

[113] F. Cascioli, S. Hche, F. Krauss, P. Maierhöfer, S. Pozzorini, and F. Siegert, Precise Higgs-background predictions: Merging NLO QCD and squared quark-loop corrections to four-lepton $+0,1$ jet production, J. High Energy Phys. 01 (2014) 046.

[114] G. Aad *et al.* (ATLAS Collaboration), Search for direct production of charginos and neutralinos in events with three leptons and missing transverse momentum in $\sqrt{s}=8$ TeV pp collisions with the ATLAS detector, J. High Energy Phys. 04 (2014) 169.

[115] S. Chatrchyan *et al.* (CMS Collaboration), Search for electroweak production of charginos and neutralinos using leptonic final states in pp collisions at $\sqrt{s}=7$ TeV, J. High Energy Phys. 11 (2012) 147.

[116] G. Aad *et al.* (ATLAS Collaboration), Search for new phenomena with the monojet and missing transverse momentum signature using the ATLAS detector in $\sqrt{s}=7$ TeV proton-proton collisions, Phys. Lett. B **705**, 294 (2011).

[117] G. Aad *et al.* (ATLAS Collaboration), Search for dark matter candidates and large extra dimensions in events with a jet and missing transverse momentum with the ATLAS detector, J. High Energy Phys. 04 (2013) 075.

[118] ATALS Collaboration, Search for new phenomena in monojet plus missing transverse momentum final states using 1 fb^{-1} of pp Collisions at $\sqrt{s}=7$ TeV with the ATLAS detector, Report No. ATLAS-CONF-2011-096.

[119] ATALS Collaboration, Search for new phenomena in monojet plus missing transverse momentum final states using 10 fb^{-1} of pp Collisions at $\sqrt{s}=8$ TeV with the ATLAS detector at the LHC, Report No. ATLAS-CONF-2012-147.

[120] S. Chatrchyan *et al.* (CMS Collaboration), Search for New Physics with a Mono-jet and Missing Transverse Energy in pp Collisions at $\sqrt{s}=7$ TeV, Phys. Rev. Lett. **107**, 201804 (2011).

[121] S. Chatrchyan *et al.* (CMS Collaboration), Search for dark matter and large extra dimensions in monojet events in pp collisions at $\sqrt{s}=7$ TeV, J. High Energy Phys. 09 (2012) 094.

[122] V. Khachatryan *et al.* (CMS Collaboration), Search for dark matter, extra dimensions, and unparticles in monojet events in protonproton collisions at $\sqrt{s}=8$ TeV, Eur. Phys. J. C **75**, 235 (2015).

[123] F. Krauss, R. Kuhn, and G. Soff, AMEGIC++ 1.0: A matrix element generator In C++, J. High Energy Phys. 02 (2002) 044.

[124] T. Gleisberg and F. Krauss, Automating dipole subtraction for QCD NLO calculations, Eur. Phys. J. C **53**, 501 (2008).

[125] S. Höche, S. Kuttimalai, S. Schumann, and F. Siegert, Beyond Standard Model calculations with Sherpa, Eur. Phys. J. C **75**, 135 (2015).

[126] A. Buckley, J. Butterworth, L. Lönnblad, D. Grellscheid, H. Hoeth, J. Monk, H. Schulz, and F. Siegert, Rivet user manual, Comput. Phys. Commun. **184**, 2803 (2013).

[127] M. V. Garzelli, A. Kardos, C. G. Papadopoulos, and Z. Trocsanyi, t $\bar{t}$ $W^{\pm}$ and t $\bar{t}$ Z hadroproduction at NLO accuracy in QCD with parton shower and hadronization effects, J. High Energy Phys. 11 (2012) 056.

[128] J. M. Campbell and R. K. Ellis, $t\bar{t}W^{\pm}$ production and decay at NLO, J. High Energy Phys. 07 (2012) 052.

[129] F. Maltoni, M. L. Mangano, I. Tsinikos, and M. Zaro, Top-quark charge asymmetry and polarization in $t\bar{t}W^{\pm}$ production at the LHC, Phys. Lett. B **736**, 252 (2014).

[130] M. Czakon, P. Fiedler, and A. Mitov, The Total Top Quark Pair Production Cross Section at Hadron Colliders through $O(\alpha_S^4)$, Phys. Rev. Lett. **110**, 252004 (2013).

[131] T. Gehrmann, M. Grazzini, S. Kallweit, P. Maierhöfer, A. von Manteuffel, S. Pozzorini, D. Rathlev, and L. Tancredi, W^+W^- Production at Hadron Colliders in Next to Next to Leading Order QCD, Phys. Rev. Lett. **113**, 212001 (2014).